

# SOLPS-ITER validation with TCV L-mode discharges

M. Wensing,<sup>1, a)</sup> H. Reimerdes,<sup>1</sup> O. Février,<sup>1</sup> C. Colandrea,<sup>1</sup> L. Martinelli,<sup>1</sup> K. Verhaegh,<sup>2</sup> F. Bagnato,<sup>1</sup> P. Blanchard,<sup>1</sup> B. Vincent,<sup>1</sup> A. Perek,<sup>3</sup> S. Gorno,<sup>1</sup> H. de Oliveira,<sup>1</sup> C. Theiler,<sup>1</sup> B. P. Duval,<sup>1</sup> C. K. Tsui,<sup>4</sup> M. Baquero-Ruiz,<sup>1</sup> M. Wischmeier,<sup>5</sup> the TCV team,<sup>b)</sup> and the MST1 team<sup>c)</sup>

<sup>1)</sup>École Polytechnique Fédérale de Lausanne (EPFL), Swiss Plasma Center (SPC), CH-1015 Lausanne, Switzerland.

<sup>2)</sup>Culham Sci Ctr, CCFE, Abingdon OX14 3DB, Oxon, United Kingdom of Great Britain and Northern Ireland.

<sup>3)</sup>Dutch Institute for Fundamental Energy Research, De Zaale 20, 5612 AJ Eindhoven, Netherlands

<sup>4)</sup>Center for Energy Research (CER), University of California-San Diego (UCSD), La Jolla, California 92093, USA.

<sup>5)</sup>Max-Planck-Institut für Plasmaphysik, 85748 Garching bei München, Germany.

(Dated: 1 September 2022)

This work presents a quantitative test of SOLPS-ITER simulations against TCV L-mode experiments. These simulations account for drifts, currents, kinetic neutrals and carbon impurities providing the most complete edge transport simulations for TCV to date. The comparison is performed on nominally identical discharges carried out to assess the effectiveness of TCV’s divertor baffles in the framework of the European PEX program (*Plasma EXhaust*) and employs numerous edge diagnostics providing a detailed code-experiment benchmark for TCV. The simulations show qualitative consistency, but quantitative differences remain that are assessed herein. It is found that, for a given separatrix density, the simulations most notably yield a colder, and denser, divertor state with higher divertor neutral pressure than measured.

## I. INTRODUCTION

Divertor power exhaust remains a key challenge on the tokamak path towards fusion energy. The design and operation of future fusion devices requires a reliable predictive scrape-off layer model. The SOLPS code has already been used in the design of the ITER divertor<sup>1</sup>. Repeated tests of the code on present-day devices, e.g. on AUG and JET<sup>2</sup>, remain crucial as any revisions of the model will bear consequences for the operation of ITER and affect the design of next step devices.

This work aims to contribute to the validation of the SOLPS-ITER code by making a stringent comparison with L-mode experiments on the *tokamak à configuration variable* (TCV). In particular the plasma-neutral interaction model is challenged following results from TCV’s divertor upgrade<sup>3,4</sup>. The TCV divertor upgrade is centered around the installation of divertor gas baffles to diminish the transit of recycling neutrals to closed flux surfaces, permitting an increased divertor region density, thereby enhancing volumetric losses in the divertor volume. Scrape-off layer simulations with the SOLPS-ITER<sup>5</sup> and the SOLEDGE2D code<sup>6</sup> highlighted the significance of plasma-neutral interaction for the plasma state in the divertor and provided predictions that were essentially confirmed in the first baffled TCV campaign<sup>7,8</sup>. Herein, we present a quantitative comparison of state-of-the art simulations against L-mode experiments by casting the simulations for comparison with numerous edge diagnostics on TCV.

This paper is structured as follows. The setup for experiments and simulations together with the strategy for compar-

ison is outlined in section II. Section III presents a detailed code-experiment comparison for the unbaffled TCV divertor. Finally, chosen aspects of the comparison for the baffled divertor are presented in section IV.

## II. COMPARISON SETUP

### A. Experiments

The comparison employs L-mode plasma density ramps to probe the effect of SOL collisionality. Here, the line-average density  $\langle n_e \rangle_l$ , taken from the far infrared interferometer chord located at  $R = 0.903$  m (FIR), is increased by the divertor gas puffing, until a plasma disruption. Only the discharges described in section III F are performed at constant  $\langle n_e \rangle_l$ . The experiments are performed in reversed  $B_\phi$  (unfavorable to H-mode access), are Ohmically heated with a plasma current of  $I_p = 250$  kA. The plasma geometry is a lower single null geometry and maintained for all discharges, cf. Figure 1a. The connection lengths from the outer midplane to the inner and outer target are  $L_{||}^i \approx 13$  m and  $L_{||}^o \approx 12$  m (evaluated 5 mm from the separatrix), respectively. The corresponding poloidal flux expansions at the targets are  $f_{exp}^i = 1.8$  and  $f_{exp}^o = 3.0$ .

These discharges were designed to experimentally assess the effectiveness of the new divertor baffles within the framework of the European PEX program (*Plasma EXhaust*) with frequent repetitions and are well-diagnosed with a wide set of edge-relevant diagnostics. The experimental database provides a strong testbed for SOLPS-ITER simulations permitting broad and stringent comparisons together with a study of experimental reproducibility.

The large experimental data set of identically programmed discharges also allows the study of experimental reproducibility. A high level of reproducibility on TCV edge experiments

<sup>a)</sup>Corresponding author: mirko.wensing@web.de

<sup>b)</sup>See the author list of S. Coda et al 2019 *Nucl. Fusion* **59** 112023.

<sup>c)</sup>See the author list of B. Labit et al 2019 *Nucl. Fusion* **59** 086020.

was previously reported by Verhaegh in experiments during a single operational day for spectroscopic measurements<sup>9</sup> (section 4.4). In the following, it will be shown that our discharges, separated in time by weeks or months, display significant variation as was also discussed in<sup>8</sup>. This complicates any comparison with numerical simulations as parameters, evidently not controlled experimentally, affect the plasma state. This is, to first order, attributed to machine conditioning, i.e. impurity content, and may be expected to change, for example, with the number and type of discharges since the preceding boronisation. Discharges directly after boronisations already show significant scatter, even when performed on the same operational day (e.g. discharges 67681, 67683). The underlying reason for this experimental variation remains elusive. Therefore, the approach taken herein is to reproduce and explain systematic experimental trends and identify possible shortcomings in the simulations rather than to reproduce the details in single experiments.

Many upgraded diagnostics are included: baratron pressure gauges to assess divertor neutral pressure (BAR), gold-foil bolometers to assess radiation (BOLO), Thomson-scattering for density and temperature profiles (TS), charge-exchange recombination spectroscopy to assess the  $C^{6+}$ -density and temperature (CXRS), vertical and horizontal infrared camera systems to assess target heat fluxes (VIR, HIR), many Langmuir probes (LP) and the divertor spectroscopy system (DSS). TCV's reciprocating probe (RCP) was not available at the midplane port for these discharges and the plasma shape was incompatible with the reciprocating divertor probe array (RDPA). An analysis using these simulations and the novel MANTIS diagnostic is given in<sup>10</sup>.

## B. SOLPS simulations

The SOLPS-ITER<sup>11,12</sup> simulations were carried out with code version 3.0.6. These account for drifts, electric currents, carbon impurities and kinetic neutrals complementing previous simulations for TCV where drift effects were neglected<sup>5,6</sup>. Drift effects in TCV simulations were found to significantly affect cross-field transport, even in presence of anomalous transport<sup>13</sup>, and electric fields in dissipative divertor conditions<sup>14</sup>.

A common set of working assumptions is employed for all presented simulations:

- The anomalous transport coefficients for radial particle diffusion and heat conduction are chosen spatially constant as a physics model for anomalous transport is unavailable. We employ  $D_{\perp}^{AN} = 0.2 \text{ m}^2/\text{s}$  and  $\chi_{\perp}^{AN} = 1.0 \text{ m}^2/\text{s}$  that reproduce the typical experimental upstream density and temperature falloff-lengths in the simulations, cf. section III A.
- Carbon impurities are introduced via physical and chemical sputtering on all plasma-facing components (PFCs). Physical sputtering follows the Roth-Bohdansky formula<sup>15</sup> and is typically small w.r.t. chemical sputtering where a yield of 3.5% is assumed.

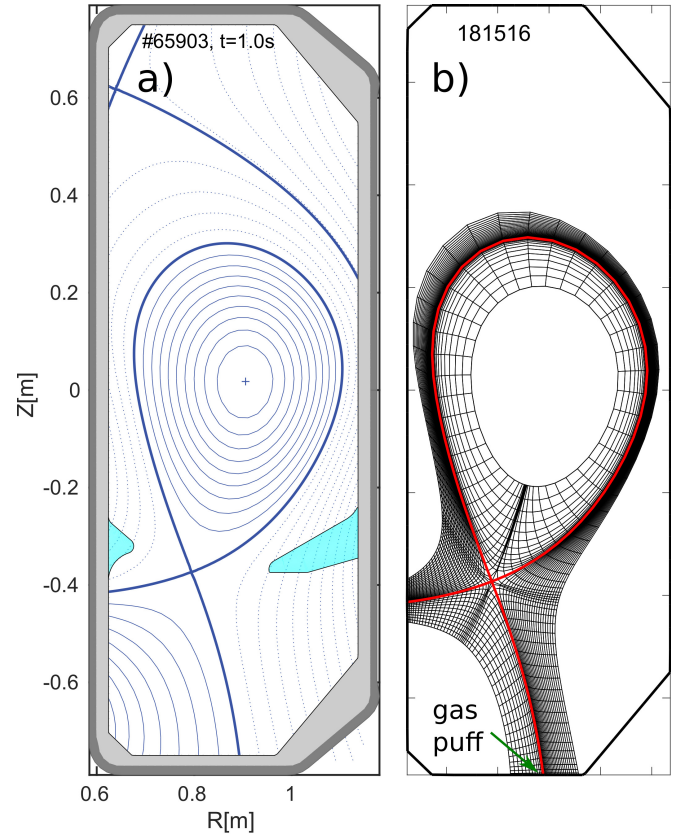


FIG. 1. a) TCV magnetic equilibrium (divertor baffles in cyan), b) corresponding SOLPS-ITER fluid grid

These values yield SOL radiation levels comparable to experimental observations, cf. section III D

- Wall-pumping is assumed with a species-independent particle recycling coefficient  $R = 1 - p_{pump} = 0.99$  on all PFCs (including divertor targets). This choice leads to gas fuelling rates comparable to the time-averaged rates in TCV discharges.
- The heating power crossing the computational core boundary is distributed equally between electrons and ions  $P_e^{core} = P_i^{core} = 165 \text{ kW}$  chosen to match the power crossing the separatrix, cf. section III D 2

The only parameter varied in these simulations is the gas puff strength that controls the upstream density  $n_e^{sep,u}$ . The particle flux over the core boundary is set to zero, i.e. the flux of deuterium ions leaving the core is equal and opposite to the inflowing deuterium neutral particle flux. For further details on simulation settings see<sup>5</sup>.

## C. Strategy for comparison

An ordering parameter is required to assign a particular experimental time during the density ramp of each discharge to a particular simulation.

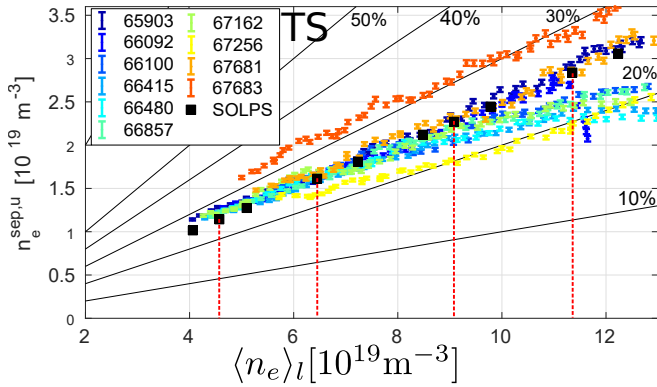


FIG. 2. Separatrix density upstream  $n_e^{sep,u}$  inferred by Thomson scattering at the lower intersection with the separatrix as function of line-averaged density  $\langle n_e \rangle_l$ . The relation  $n_e^{sep,u} \approx 0.25 \langle n_e \rangle_l$  is used to attribute a value of  $\langle n_e \rangle_l$  to each simulation. Red dashed lines mark the positions where profiles are compared in the following.

The line-averaged density  $\langle n_e \rangle_l$  will be used as the ordering parameter. Experimentally,  $\langle n_e \rangle_l$  is measured by the FIR along a vertical chord passing through the plasma core. The simulation does not access  $\langle n_e \rangle_l$  as the plasma core is not modelled. The experimental relation between  $n_e^{sep,u}$  and  $\langle n_e \rangle_l$ , Figure 2, can, nevertheless, be used to attribute a line-averaged density to each simulation such that the average experimental upstream density coincides with the simulations. Here, the upstream separatrix density  $n_e^{sep,u}$  is inferred at the lower TS-separatrix intersection where TS has sufficient spatial resolution in the SOL. The TS polychromators at the upper separatrix intersection, designed for high  $T_e$  conditions, yield poor data quality in the edge and were omitted. TS data within the time window of  $[-50, +50]$  ms and a region of  $[-1, +1]$  cm around the separatrix location is used to define the separatrix values of electron density  $n_e^{sep,u}$ , temperature  $T_e^{sep,u}$  and pressure  $p_e^{sep,u}$  using a linear least square fit. For the TCV PEX discharges we empirically find

$$n_e^{sep,u} \approx \begin{cases} 0.25 \langle n_e \rangle_l & \text{unbaffled divertor} \\ 0.30 \langle n_e \rangle_l & \text{baffled divertor} \end{cases} \quad (1)$$

for the unbaffled, Figure 2, and the baffled divertor, Figure 18. Discharges without baffles reached higher  $\langle n_e \rangle_l$  than baffled cases that is likely linked to increased core ionisation without baffles.

The evolution of the upstream density  $n_e^{sep,u}$ , Figure 2, shows low experimental scatter for low  $\langle n_e \rangle_l$  whereas deviations occur at high density, where some discharges (#66092) feature a roll-over in  $n_e^{sep,u}$  near  $\langle n_e \rangle_l \approx 9.5 \cdot 10^{19} \text{ m}^{-3}$ , approximately 100 ms before the final disruption. This roll-over is considerably more pronounced in baffled shots and will be discussed in section IV A. It should be noted that the simulated  $n_e^{sep,u}$  increases monotonically with increasing gas puff (i.e. roll-over is absent). The large scatter of  $n_e^{sep,u}$  and its roll-over impede the use of  $n_e^{sep,u}$  as an ordering parameter for the comparison.

The non-stationary plasma density in these experiments (density ramp rates  $d\langle n_e \rangle_l/dt \approx 6 \cdot 10^{19} \text{ m}^{-3}/\text{s}$ ) raises the

question as to the influence of the ramp rate on the plasma state and, to what extent, a comparison with stationary simulations is appropriate. The discharges at constant plasma density  $\langle n_e \rangle_l$ , cf. section III F, feature upstream densities  $n_e^{sep,u}$  that are  $\sim 10\%$  lower than corresponding density ramp discharges in Figure 2 (not shown). This deviation is attributed to the finite particle transport time scale  $\tau_p$  for increasing the core density by perpendicular transport following increased ionisation in the edge region. For TCV, we estimate the transport time as  $\tau_p \approx a^2/D_{\perp}^{AN} \sim 0.2 \text{ s}$ , with minor radius  $a = 0.2 \text{ m}$  and particle diffusivity  $D_{\perp}^{AN} = 0.2 \text{ m}^2/\text{s}$ , by taking the anomalous diffusivity near the separatrix from the simulations for a crude estimate. The density ramp introduces another time scale,  $\tau_{ramp} = \langle n_e \rangle_l / |d\langle n_e \rangle_l/dt| \approx 1 \text{ s}$ , such that deviations between discharges at constant density and density ramps may be expected as  $\tau_{ramp} \sim \tau_p$ . Hence, it is important to note that the line-averaged density  $\langle n_e \rangle_l$ , by itself, is not always a suitable ordering parameter and choosing (1) for the comparison is herein justified by the resulting reasonable match in the average upstream profiles, cf. section III A.

### III. COMPARISON - UNBAFFLED TCV

The diagnostic availability for all considered discharges without divertor baffles is summarised in Table Ia with the corresponding SOLPS-ITER simulations, for a range of densities obtained by varying the gas puff, listed in Table Ib.

The comparison includes upstream plasma parameters, section III A, target plasma parameters, section III B, divertor neutral pressure, section III C, radiation profiles and impurity densities, section III D, and spectroscopic measurements, all analysed for density ramp experiments, section III E. Additional experiments, at constant density, aim to simultaneously compare electron density and temperature profiles at several poloidally-separated positions in the SOL, section III F.

#### A. Upstream plasma parameters and profiles

The upstream density  $n_e$  and temperature  $T_e$  profiles are taken from Thomson scattering at the lower intersection between separatrix and the TS laser path. Empirical anomalous transport coefficients are chosen to best match the experimental profiles (within experimental scatter) for these L-mode plasmas, Figure 3a-h. Spatially constant transport coefficients are found sufficient to approximate the experimental profiles in the SOL. The agreement is worse on closed flux surfaces and worsens into the plasma core. This is, however, not thought to invalidate the comparison in the SOL as the core only affects the SOL parameters through the fluxes across the separatrix.

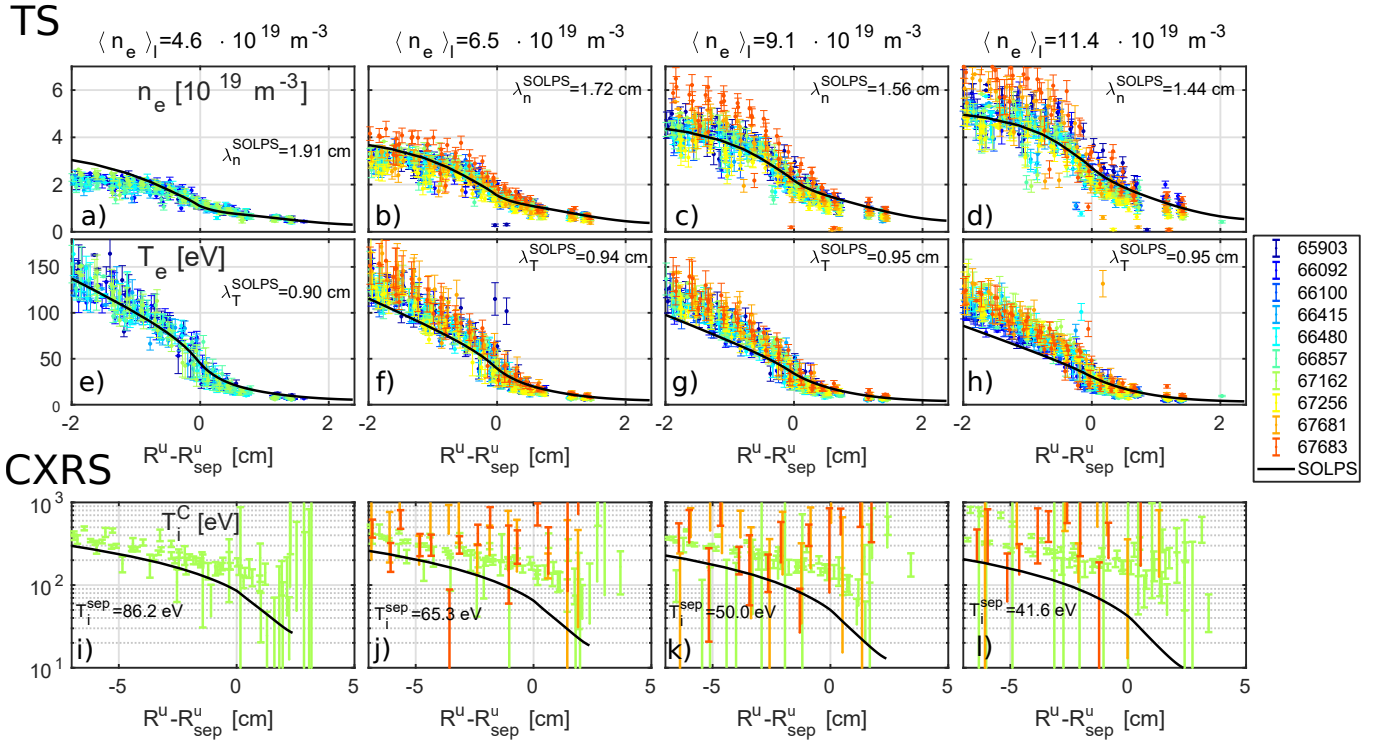
CXRS is used to measure the ion temperature in the core-edge region. The simulated  $T_i$  appears to be underestimated, Figure 3, although one should note the with relatively large experimental uncertainties in the SOL. Nevertheless, simulations and experiments consistently find an ion temperature that exceeds the electron temperature,  $T_i^u > T_e^u$ .

## a) PEX experiments - no baffle

#shot	BAR	BOLO	TS	CXRS	VIR	HIR	LP	RCP	RDPA	DSS	MANTIS
65903	green	green	green	red	red	red	green	red	red	red	green
66092	green	green	green	red	green	green	green	red	red	red	green
66100	green	green	green	red	green	green	green	red	red	red	green
66415	green	red	green	red	green	green	green	red	red	red	green
66480	green	red	green	red	green	green	green	red	red	red	green
66857	green	red	green	red	green	green	green	red	red	red	green
67162	green	red	green	red	green	green	green	red	red	red	green
67256	green	red	green	red	green	green	green	red	red	red	green
67681	green	red	green	red	green	green	green	red	red	red	green
67683	green	red	green	red	green	green	green	red	red	red	green

## b) SOLPS simulations - no baffle

gas puff $\Gamma_{D_2}$ [ $10^{20}$ D <sub>0</sub> /s]	1.5	2	3	4	5	6	7	8	10	12	15
$n_e^{sep,omp}$ [ $10^{19}$ m <sup>-3</sup> ]	1.02	1.14	1.27	1.61	1.81	2.12	2.27	2.46	2.86	3.07	3.80
MDS number	181516	179196	161457	179182	176913	179181	178560	181757	181751	181759	181758

 TABLE I. a) Diagnostic availability in TCV discharges without baffles: red=no data available, green=data acquired, b) SOLPS-ITER density scan with separatrix density at the outer midplane  $n_e^{sep,omp}$  and MDS number.

 FIG. 3. a)-d) TS electron density  $n_e$  and e)-f) TS electron temperature  $T_e$ , i)-l) CXRS ion temperature  $T_i$  measurements during density ramp

The dependence of upstream electron temperature  $T_e$  and static pressure  $p_e = n_e T_e$  on plasma density is shown in Figure 4. Interestingly,  $T_e^{sep,u}$  decreases during a density ramp, whereas no change is expected from the basic, conductive, two-point model<sup>16</sup>. The dependence is, however, readily reproduced in SOLPS-ITER simulations that is attributed to an increased heat convection as the divertor cools with increasing plasma density. The static electron pressure  $p_e^{sep,u}$ , however, increases with plasma density. Only discharges #65903 and #66092 feature a deviation of the simulated trend where  $T_e^{sep,u}$

and  $p_e^{sep,u}$  decrease sharply before the disruption (see section IV A). Discharges #67681 and #67683 were performed shortly after a boronisation and feature higher  $T_e^{sep,u}$  and  $p_e^{sep,u}$  for a given  $\langle n_e \rangle_l$  with respect to the other discharges, indicating that the impurity content influences the upstream parameters.

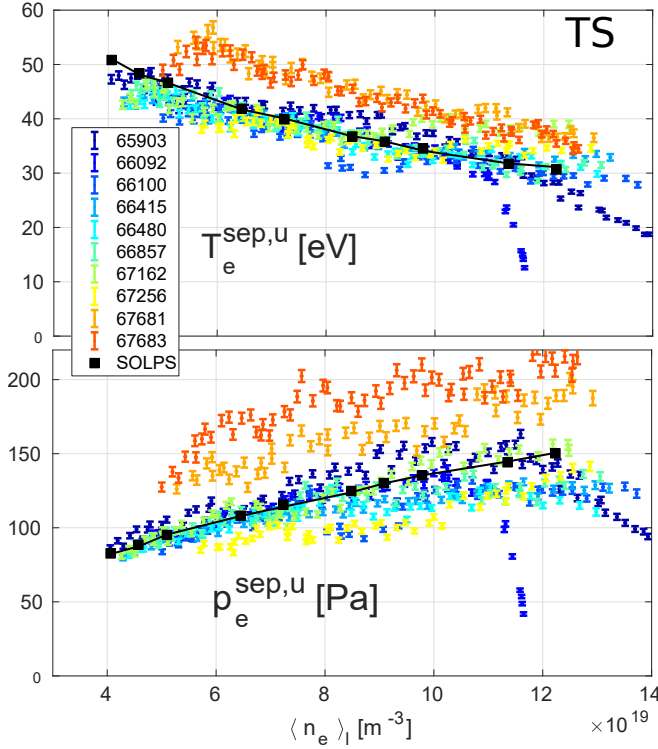


FIG. 4. Comparison of the density dependence of upstream electron temperature  $T_e$  and static electron pressure  $p_e$

## B. Target plasma parameters and profiles

Target plasma parameter measurements for particle flux  $j_{sat}^\perp/e$ , heat flux  $q_\perp$  (both evaluated perpendicular to the target normal), electron density  $n_e$  and electron temperature  $T_e$  are provided by the TCV wall-mounted voltage-swept Langmuir probes and infrared cameras.

### 1. Target particle flux

The target particle fluxes are directly related to the volumetric particle sinks and sources in the plasma

$$I_{it} + I_{ot} \approx \int S_{part} dV \quad (2)$$

providing a direct comparison to the simulated particle balance. The target particle flux profile shapes and their in/out asymmetries are influenced by the spatial distribution of the particle source and transport parallel and perpendicular to the magnetic field direction. The simulated target particle flux profiles  $j_{sat}/e$  and their integrals are compared for both targets, Figures 5 and 6.

The simulated profile shape at the inner target is consistent with LP measurements, but its structure (e.g. the double-peaked profiles at the inner target at low density that have been observed in previous TCV experiments<sup>17</sup>) cannot be verified in these experiments without strike point sweeping due to the spatial separation of the LPs ( $\sim 2$  cm) at the inner wall. The

simulated outer target  $j_{sat}$  profile is more symmetric than measured where a steep flank towards the PFR region prevails. At the inner target, the simulated particle flux amplitude is overestimated by up to  $\sim 50\%$  for medium densities but matches better for high densities. At the outer target, the simulated particle flux amplitude matches reasonably well with the LP data within the experimental scatter. Also the integrated particle flux, including the in/out asymmetries, is reasonably well reproduced by the simulations, Figure 6, with the exception of the inner target, again only for medium densities. Note, that the integrated particle flux is prone to uncertainty originating from the low spatial resolution of LPs at the inner wall.

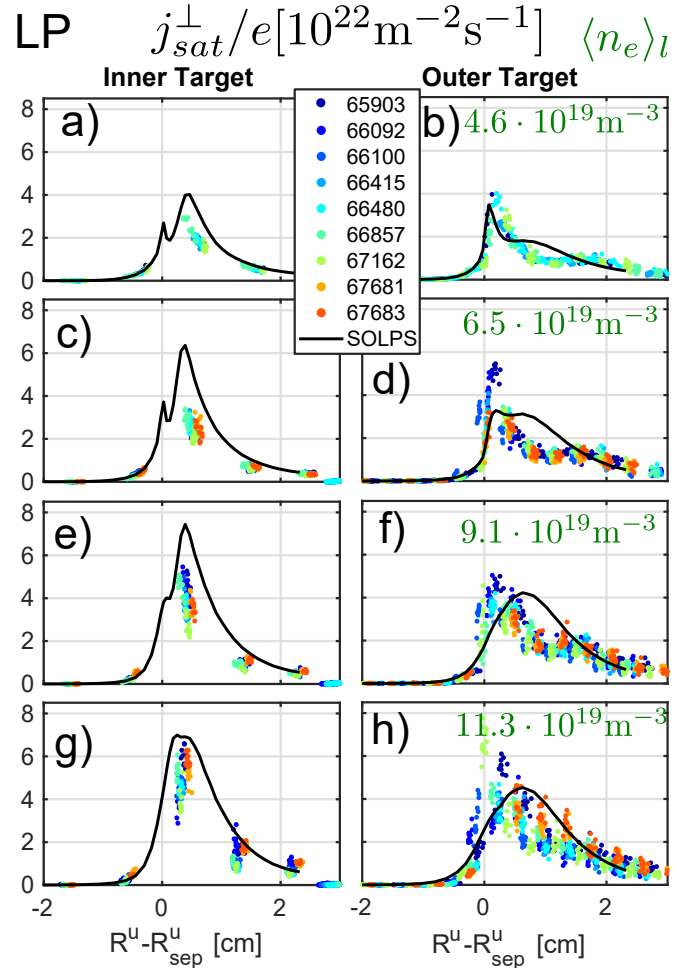


FIG. 5. Comparison of inner and outer target particle flux profiles employing wall-mounted LPs

Note, that neither experiment nor simulations feature a clear roll-over of the particle flux at the inner or outer targets. An outer-target roll-over is only observed in #65903 and #66092, the discharges with upstream pressure drops. In section III E it is demonstrated that the absence of a roll-over is consistent with spectroscopic measurements that indicate little volumetric recombination.

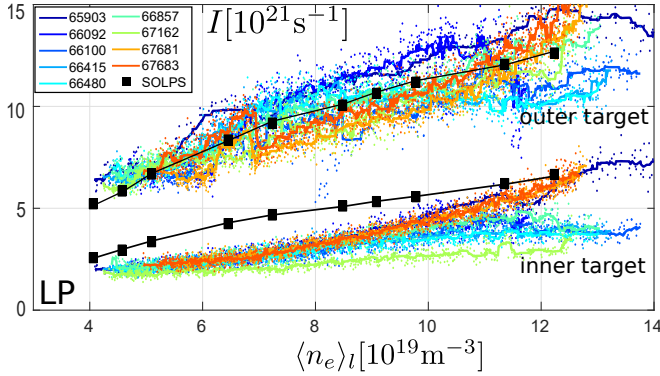


FIG. 6. Comparison of inner and outer target particle flux profiles employing wall-mounted LPs

## 2. Target heat flux

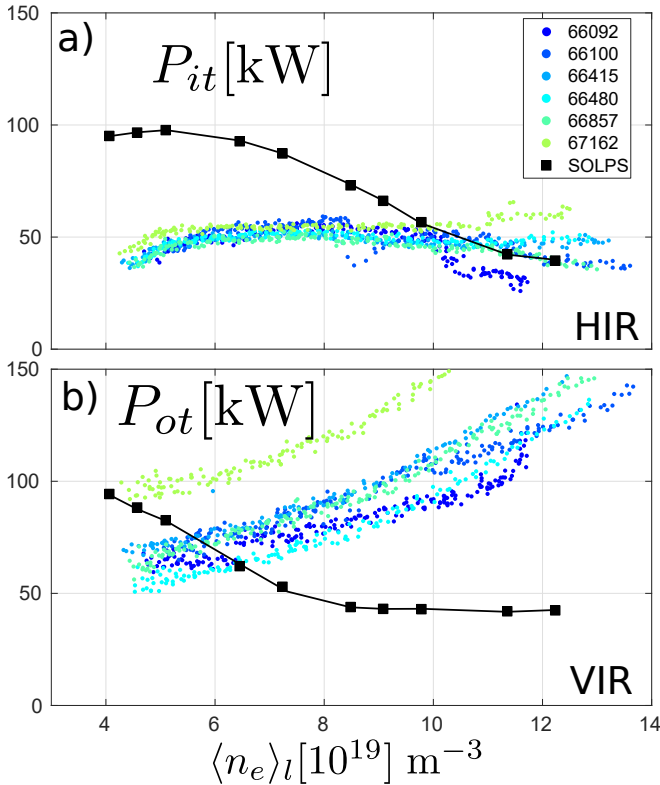


FIG. 7. Comparison of power to the outer and inner target (infrared cameras)

The deposited power at both targets is related to the radiation losses in the plasma

$$P_{it} + P_{ot} \approx P_{SOL} - \int Q_{rad}^{SOL} dV \quad (3)$$

providing a test of the simulated  $P_{SOL}$  and SOL radiation. Note, ionisation and dissociation do not directly contribute

to (3) as the involved energy is retained as potential energy within the plasma and is redeposited at the targets, whereas the thermal energy density of the plasma is locally reduced. Equation (3) furthermore assumes that neutral particle heat loads towards PFCs remote from the targets are negligible. Target heat flux profiles, and their in/out asymmetries, are also influenced by the spatial distribution of volumetric power sinks and heat transport parallel and perpendicular to the magnetic field direction.

The simulated power to the inner target  $P_{it}$  exceeds the experimental infrared camera measurements at low plasma density but agrees reasonably well at high density, Figure 7a. The IR system viewing the inner target (HIR) indicates decreasing  $P_{it}$  with increasing density, that is predicted by simulations, albeit to a smaller extent. Contrary to the simulations, the vertical infrared camera indicates increasing  $P_{ot}$  during the density ramp, Figure 7b, which is unexpected as the SOL radiation increases from  $\sim 60$  to  $\sim 140$  kW that cannot be explained by a variation in  $P_{SOL}$  alone, cf. section III D.

The simulated target heat flux profiles  $q_{\perp}^t$  are compared at both targets using Langmuir probe (assuming sheath heat transmission coefficient  $\gamma = 5$ ) and infrared camera measurements, Figure 8. There is reasonable agreement between LPs and IR for low plasma density, recalling the limited LP resolution at the inner SP, Figure 8 a-d. However, at high density, the LP measurements clearly exceed the infrared camera heat flux, Figure 8 i-p. LPs can only account for power deposited by the plasma and the potential energy, whereas the infrared cameras are additionally sensitive to radiation and neutral heat load contributions, such that  $q_{\perp}^{IR,t} > q_{\perp}^{LP,t}$ . Simulations, however, indicate that the contribution from neutrals and radiation to the total peak heat flux is small and give rise to a near constant background level. The disagreement between LP and IR, thus, cannot be explained by these contributions. Both for LP and IR measurements, a large experimental scatter between the discharges is observed at high plasma density, even between measurements from the same diagnostic, Figure 8 m-p.

At low density, the simulated heat flux profile features a similar shape, albeit with different amplitude (factor  $\sim 4$  inner target,  $\sim 2$  outer target), compared to the experimental profile, with a steep flank towards the PFR. At high density, especially for the outer target, the simulated heat flux profile is nearly symmetric, whereas a steep flank towards the PFR prevails experimentally.

To investigate the influence of non-ambipolar flows to the total heat flux, we evaluate the heat-flux without currents, neutrals and radiation contributions  $(\gamma_e T_e' + \gamma_i T_i' + \varepsilon)\Gamma_i$ , assuming here  $\gamma_e = \gamma_i = 7/2$ , cf. red dotted line in Figure 8. At low densities the ambipolar peak heat flux is smaller by factor  $\sim 2$  than the total peak heat flux at the inner target and by  $\sim 30\%$  at the outer target. The non-ambipolar contribution becomes however small towards high densities as the peak electric currents towards the target are also reduced. In the TCV divertor the parallel current is dominated by Pfirsch-Schlüter currents, as previously presented in<sup>14</sup>.

It is thought that the infrared cameras may pick up radiation from the plasma in the divertor volume. Possible candidates for the parasitic signal are bremsstrahlung, atomic hy-

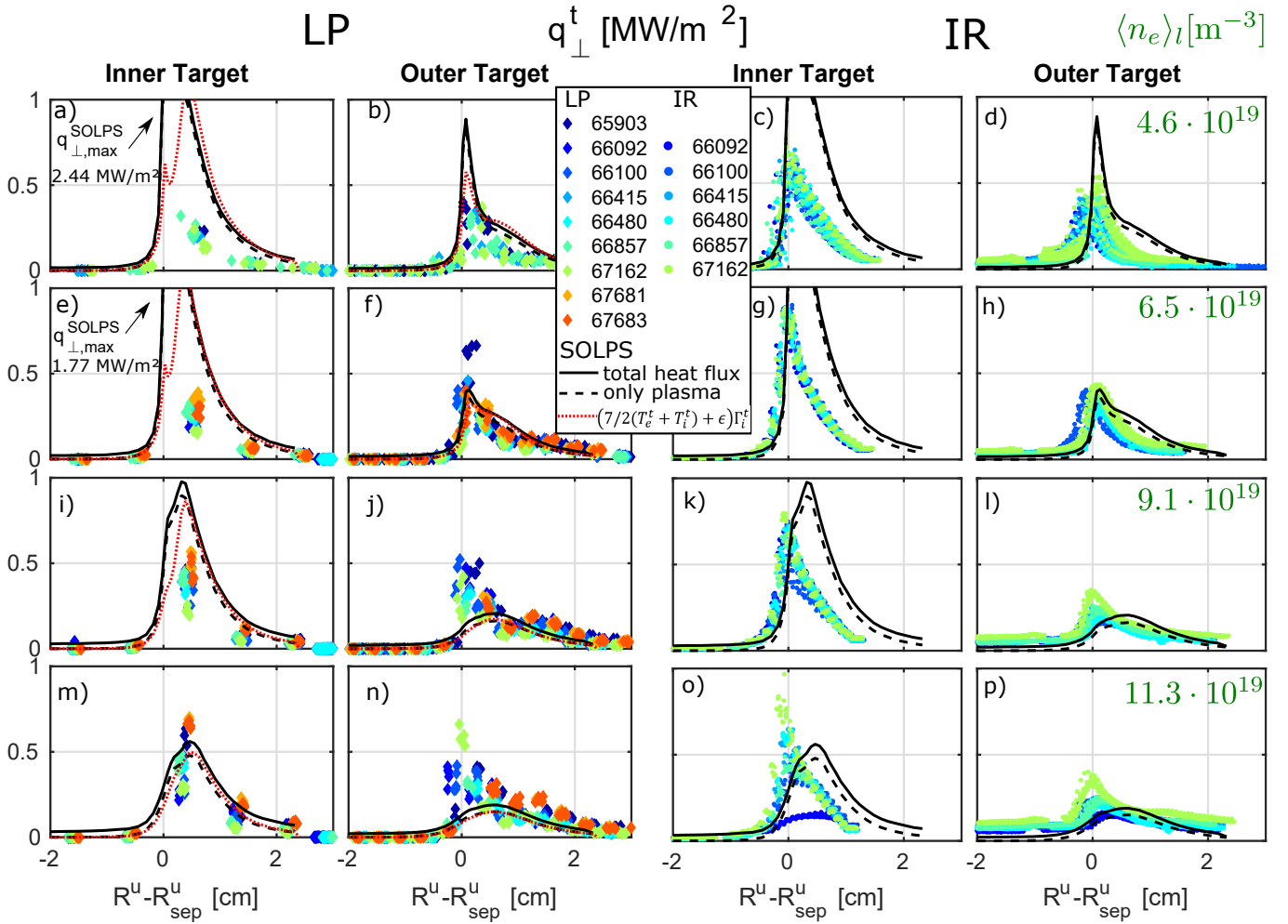


FIG. 8. Comparison of target heat flux measurements by Langmuir probes ( $\blacklozenge$ , left) and infrared cameras ( $\bullet$ , right) at the inner and outer target for various plasma densities. Solid black lines (-) indicate the total heat flux to the target, accounting for plasma, potential energy, radiation and neutral contributions. Dashed black lines (- -) correspond to the heat flux excluding neutral and radiation contributions, i.e. those contributions detectable by LPs. Red dotted lines (only left) represent the ambipolar ( $\Gamma_e^t = \Gamma_i^t$ ) heat flux, here estimated with sheath heat transmission coefficients  $\gamma_e = \gamma_i = 7/2$ .

drogen lines (Brackett ( $n \rightarrow 4$ ) and Pfund series ( $n \rightarrow 5$ )) and molecular radiation that fall into the spectral window of the VIR. This does, however, not explain the disagreement with Langmuir probes. The significance of non-ambipolar contributions in simulations may also provide a possible reason for the deviation between IR and LP heat fluxes, especially at low density. The deviation will be further investigated in future experiments.

### 3. Target electron density and temperature

Reactions between plasma species, neutrals and molecules (electron-impact excitation and resulting radiation, ionisation, recombination, dissociation etc.) are often strong functions of electron density  $n_e$  and temperature  $T_e$ . It is, hence, important to accurately match  $n_e$  and  $T_e$  in the SOL, where a reasonable match is obtained upstream, section III A.

The target electron density  $n_e^t$  is obtained from wall-mounted LPs, Figure 9. The simulated density exceeds that from the LPs by up to factor  $\sim 4$ . The measured target densities are comparable to upstream densities from TS, whereas the simulations show significantly larger values  $n_e^t > n_e^u$ . Similarly to particle flux and heat flux profiles, the simulated density profile does not recover the experimental radial asymmetry with steep flanks towards the PFR at high density. The target electron temperature  $T_e^t$  from LPs is compared to the simulation results, Figure 10. The simulated target electron temperature decreases strongly with increasing plasma density, as expected for a conduction-limited regime. Also seen experimentally, a reduction of peak target temperature is observed, albeit never below  $T_e^{t,max} \approx 7$  eV.

Notably, discharges carried out shortly after a boronization (67681 and 67683) feature systematically higher  $T_e^t$ , lower  $n_e^t$  and higher  $T_e^{sep,u}$ , cf. Figure 4. This is consistent with a lower impurity concentration, cf. section III D.

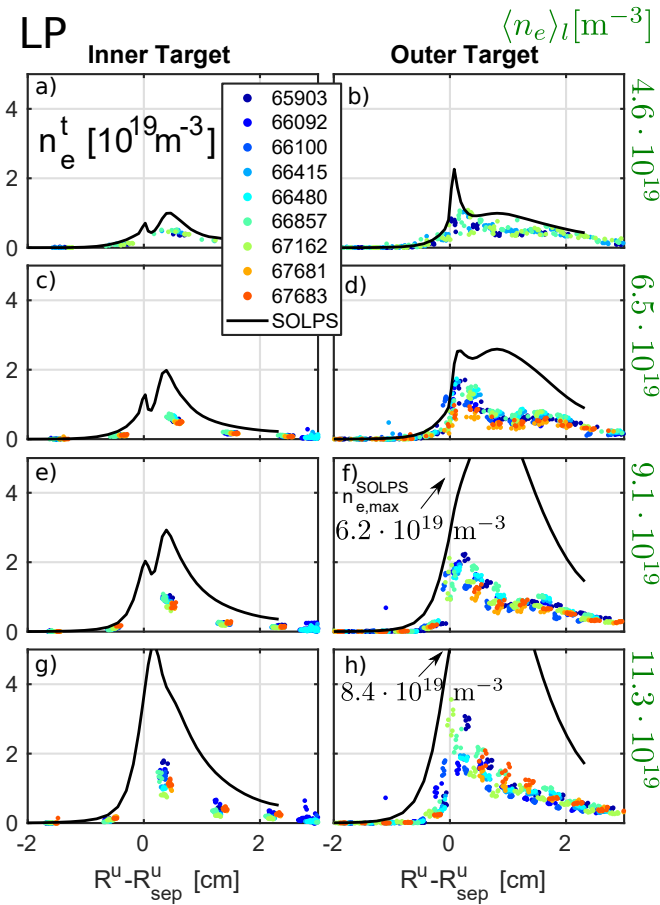


FIG. 9. Comparison of target  $n_e$  profiles employing wall-mounted LPs

In summary, the simulations correctly capture the measured particle flux to the target and its in/out asymmetries. The target heat fluxes, however, are not captured correctly. The simulation underestimates  $P_{it}$  for low plasma density and only becomes comparable at high density, whereas  $P_{ot}$  remains underestimated throughout. The disagreement between IR and LP heat fluxes, together with the unexpected experimental increase of  $P_{ot}$  (possibly from pickup of plasma radiation from the IR) raises the question of the validity of the measurements as estimates of power deposition and demands further attention. Langmuir probe measurements indicate that the simulations overestimate the density  $n_e^t$  and underestimate the temperature  $T_e^t$ . As Langmuir probes are prone to overestimate temperatures in a cold divertor due to kinetic effects, cf.<sup>18</sup>, the result may be simply a shortcoming of the measurements. Supplementary data from the DSS, section III E, divertor Thomson scattering and RCP plunges in the divertor leg aim to clarify the density and temperature discrepancy, section III F, and provide further indications that the simulated  $T_e^t$  is, indeed, underestimated.

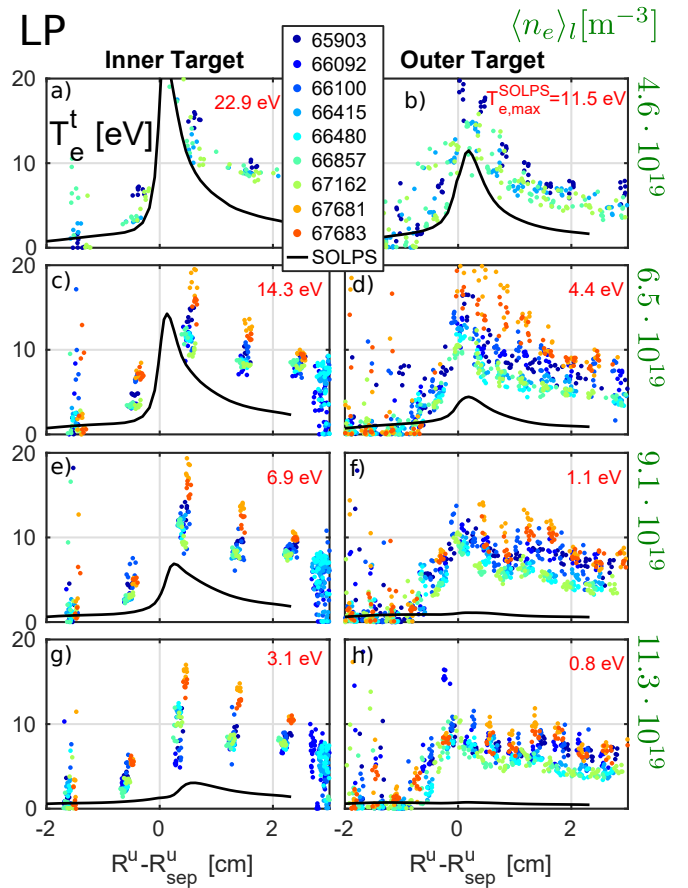


FIG. 10. Comparison of target  $T_e$  profiles employing wall-mounted LPs

### C. Divertor neutral pressure

The simulations and experiments in preparation of the TCVC divertor upgrade<sup>5,7,8</sup> demonstrate that neutral dynamics significantly affect the plasma state in the SOL.

The divertor neutral pressure  $p_n^{div}$  is measured by the divertor baratron (BAR). A synthetic baratron model, cf. section 4.1 in<sup>5</sup>, permits a direct comparison of simulated and measured neutral pressure, Figure 11. This reveals that the simulated divertor neutral pressure  $p_n^{div}$  systematically exceeds the measured value by factor  $\sim 4$  for a given line-average density  $\langle n_e \rangle_l$ .

Only discharge #65903 approached the simulation predictions reaching values of 95 mPa at the highest density, whereas all other discharges remained below 50 mPa. Discharge #65903 was one of the first TCVC discharges after the baffle installation in 2019 with sand-blasted tiles and subsequent boronisation. Comparable repeats after boronisation (#67681 and #67683) resulted, however, in the lowest divertor pressure  $p_n^{div}$  of the dataset. Hence, no clear correlation between boronisation and particularly high, or low, divertor neutral pressure is found.

The interpretation of the measurement is further complicated by the finite delay and response times of the baratrons ( $\sim 60$  ms). They are, however, insufficient to reconcile simu-

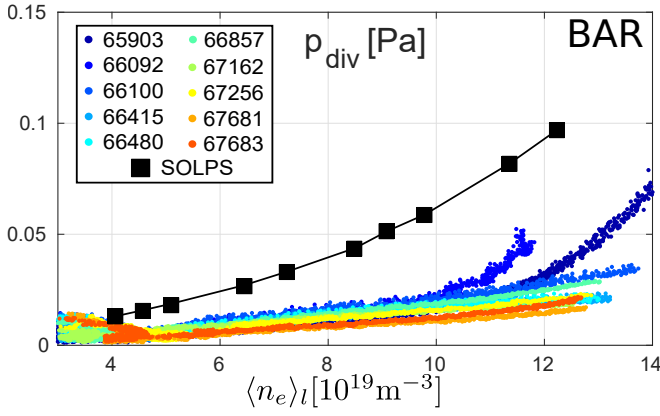


FIG. 11. Divertor neutral pressure  $p_n^{div}$  as measured by the divertor baratron gauge

lated and measured baratron pressures. Further discussion of the discrepancy is provided in context of the baffled experiments, section IV D.

#### D. Radiation and impurity content

Carbon is the main radiator in the SOL for unseeded TCV discharges and therefore an essential ingredient in its power balance. The SOL carbon content and resultant radiation is compared employing CXRS and BOLO to further assess any discrepancies between the simulated and experimental density and temperature target profiles discussed in section III B.

##### 1. Core-edge $C^{6+}$ content - CXRS

The density of fully-stripped carbon ions  $n_{C^{6+}}$  is measured by the CXRS diagnostic in the core-edge region, Figure 12.

The simulated  $n_{C^{6+}}$  ranges from  $1 - 10 \cdot 10^{16} \text{ m}^{-3}$ , i.e. nearly an order of magnitude smaller than measured in shot #67162 and only matches the carbon levels for shots taken shortly after a boronisation (#67681 and #67683). This cannot be explained by a lack of local ionisation in the simulation as  $n_e$  and  $T_e$  are reasonably matched in that region. In the simulations shown here,  $T_e$  at the core boundary is in the range 200 – 320 eV, where for a coronal equilibrium (i.e. effectively no transport) nearly all carbon should be fully stripped. Also in the simulation, the fractional abundance of  $C^{6+}$  ranges from 50 and 80% near the core boundary. Even the total carbon content, i.e. accounting for all ionisation states, is lower by factor  $\sim 4$  w.r.t to CXRS measurements 5 cm from the separatrix, but becomes comparable to CXRS measurements near the separatrix. In practice, recombination of  $C^{6+}$  is negligible in the corresponding area for the simulation. The discrepancy can possibly be explained noting that carbon  $C^{6+}$  production in the simulation only occurs locally through ionisation, a radial outflux of  $C^{6+}$  across the core boundary is not permitted as the core boundary particle flux is set to zero for all plasma species.  $C^{6+}$  can then only be created in the 5 cm broad region

around the core boundary while outflux from regions deeper from the core is neglected.

The density estimates of the CXRS depend inversely on the neutral density from the neutral beam (Equation 2.10 in<sup>19</sup>). Spatial misalignment between the CXRS lines of sight and the DNBI beam would hence yield an overestimated carbon measurement. An order of magnitude error is, however, considered very unlikely.

Contrary to the CXRS results upstream, the following will indicate that the simulated carbon content is to be overestimated in the divertor.

##### 2. SOL radiation - BOLO

Bolometers provide line-integrated measurements of incident power from neutrals and radiation [ $\text{W}/\text{m}^2$ ] along chords displayed in Figure 13a. The measurements can be compared to the radiated power in the scrape-off layer  $P_{rad}^{SOL}$ , with the assumption that the neutral contribution to the measurement is negligible, and thus provide another measure of the influence of SOL impurity content. Furthermore, an estimation of the power crossing the separatrix can be made, from  $P_{SOL} = P_{Ohm} - P_{rad}^{core}$  where  $P_{Ohm}$  is the Ohmic heating power and  $P_{rad}^{core}$  the radiated power in the core region from the tomographic inversion of BOLO measurements.

The Ohmic heating increases during a density ramp that is partially compensated by enhanced core radiation. The power crossing the separatrix  $P_{SOL}$  increases with density from approximately 270 kW to 350 kW, Figure 13b. The simulated  $P_{SOL}$  stays approximately constant at  $\approx 300$  kW for the choice of  $P_{core} = 330$  kW supplied over the core boundary. Variations of  $P_{SOL}$  of  $\pm 10\%$  were found to have little effect on the simulated target parameters and were insufficient to reconcile deviations in target parameters discussed above (not shown).

The radiated power is evaluated from the bolometry tomographic inversion in the SOL and core regions and can be delimited between core and SOL radiation using the LIUQE equilibrium reconstruction. A certain amount of caution is required as this method is highly prone to uncertainties in the separatrix position. Both in simulations and experiments  $P_{rad}^{SOL}$  increases with plasma density 13c. The dominant radiated power fraction in the simulation is given by  $C^{2+}$  and  $C^{3+}$  from their excitation emission through electron impact that is sensitive to the local electron temperature  $T_e$  that, itself, increases linearly with density  $n_e$ . The comparison of  $P_{rad}^{SOL}$  provides a test of the simulated carbon source from wall sputtering as the radiated power is linked to the carbon density. The simulated radiation is overestimated by up to 50% for low and medium plasma densities up to  $\langle n_e \rangle_l \approx 9 \cdot 10^{19} \text{ m}^{-3}$ , whereas simulated and measured  $P_{rad}^{SOL}$  agree within the experimental scatter for high density. The radiated power, hence, indicates an overestimated divertor carbon density and/or more favorable divertor conditions for carbon to radiate, e.g. overestimated  $n_e$ .

To investigate the spatial distribution of the radiation in the SOL, synthetic bolometers were developed for TCV's SOLPS simulations. The simulated radiated power density  $Q_{rad} [\text{W}/\text{m}^3]$  is integrated along coordinate  $s$  of the lines of

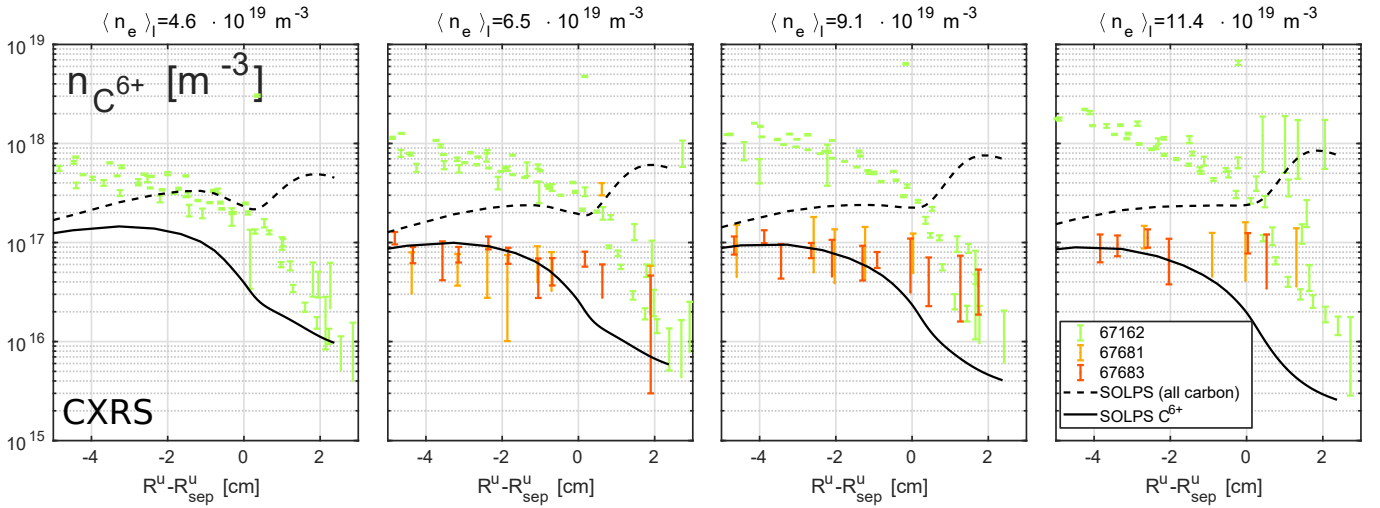


FIG. 12. CXRS measurements of fully stripped carbon in the edge region, discharges 67162 was taken several weeks after a boronisation, 67681 and 67683 were taken a few days after a boronisation

sight of each of the 64 bolometer chords

$$q_{foil} = \int Q_{rad} ds. \quad (4)$$

To account for the finite étendue of bolometer chords each viewing cone is subdivided into 50 sub-chords and averaged. The opening angle of the cone is equal to half the angular difference to adjacent chords. This technique allows direct comparison with calibrated bolometric chord brightnesses [ $\text{W}/\text{m}^2$ ], Figure 13d-g, without relying on tomographic inversions that were insufficient to resolve known features in the radiation profile<sup>9</sup> (section 4.3.1).

The synthetic bolometer, Figure 13d-g, shows remarkable agreement with the TCV data confirming the spatial distribution of the simulated radiation profile. Discrepancies are visible in the bottom camera channel for all densities (red shaded area) where the simulated chord brightness exceeds the measured values. This deviation again decreases for higher plasma density.

The synthetic bolometer thus confirms the trend observed in Figure 13c indicating an overestimated  $P_{rad}^{SOL}$  at low and medium plasma density and enables us to attribute the mismatch to the divertor region. From the comparison it is, however, not clear whether the divertor carbon content is overestimated or the plasma conditions are more favorable to promoting carbon radiation. Such increased carbon radiation would possibly be related to the higher  $n_e$  and lower  $T_e$  in the simulations as indicated by LPs, section III B.

### E. Spectroscopic comparison

Spectrally resolved emission from the divertor region is measured by the DSS. It enables a further comparison of the divertor plasma state and the underlying atomic processes between experiment and simulation from Balmer and Carbon spectral line emission measurements.

### 1. Balmer lines

Balmer line emissivities depend on the electron density  $n_e$ , electron temperature  $T_e$ , the deuterium ion density  $n_{D^+}$  (recombination emission) and the deuterium atomic neutral density  $n_{D^0}$  (excitation emission) under the assumption of negligible molecular contributions and can be evaluated from the simulation following the ADAS database<sup>20</sup>. Spectroscopic measurements can therefore probe the divertor plasma conditions with high sensitivity and provide an ideal testbed for the simulations. Balmer line intensities become increasingly influenced by volumetric recombination as a function of primary quantum number  $n$  as recombination reactions tend to populate higher  $n$  levels w.r.t. electron impact excitation. Therefore, the ratio between Balmer line brightnesses of different upper  $n$  transitions can be used as an indicator for the excitation to recombination ratio. A quantitative separation of the recombinative and excitative contributions from TCV Balmer lines was first applied by Verhaegh<sup>9,21</sup> (section 7.2).

The comparison employs the DSS diagnostic view lines after its 2019 upgrade and covers both divertor legs. DSS measurements of  $D_{5 \rightarrow 2}$ ,  $D_{6 \rightarrow 2}$  and  $D_{7 \rightarrow 2}$  line brightnesses are taken for the unbaffled discharges, Figure 14. The line-integrated DSS measurements correspond to the viewing chords intercepting the outer divertor leg, numbered in ascending order from the outer strike point towards the X-point. A synthetic DSS estimation follows the same methodology as that for the synthetic bolometers, cf. section III D 2, for a direct comparison with measurements.

The measured and the synthetic DSS chord brightnesses generally reveal two distinct peaks corresponding to the outer and inner strike point. The absolute value of the Balmer line brightness is overestimated near the strike points and suggests a locally overestimated density, whereas the data agrees quantitatively along the outer divertor leg, within the experimental scatter, for medium plasma densities, Figure 14 b,c,f,g. The measured Balmer line signals show little variation with

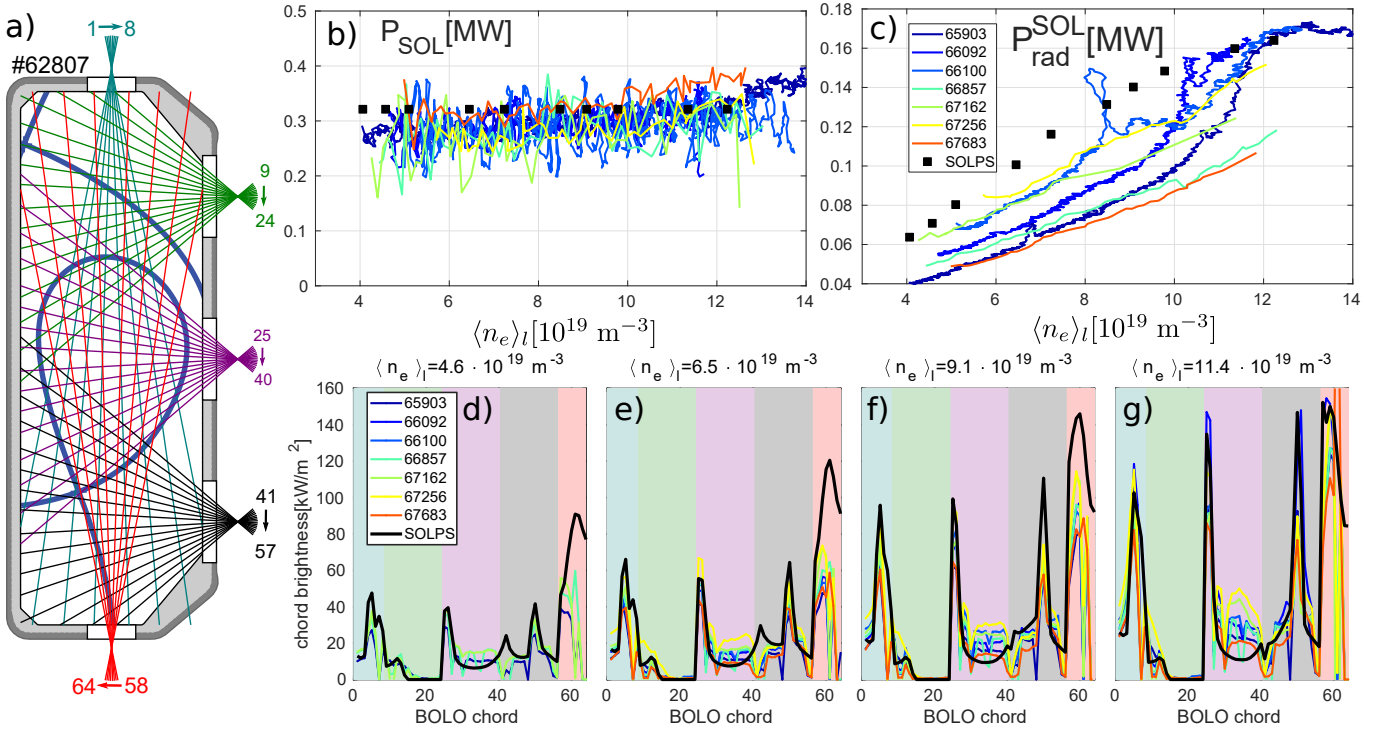


FIG. 13. a) bolometer coverage, b) estimated power crossing the separatrix  $P_{\text{SOL}} = P_{\text{Ohm}} - P_{\text{rad}}^{\text{core}}$ , c) power radiated in the SOL  $P_{\text{SOL}}^{\text{rad}}$ , d-g) evolution of line-integrated absorbed power per channel during the density ramp. Shaded areas correspond to the top (blue), upper lateral (green), midplane lateral (purple), lower lateral (black) and bottom BOLO cameras (red).

increasing plasma density, whereas the simulations predict strongly increased  $D_{6 \rightarrow 2}$  and  $D_{7 \rightarrow 2}$  emission near both strike points due to increasing recombinative contributions to the respective Balmer lines that is indicative of an underestimated electron temperature in the simulation.

Balmer line ratios confirm that the outer divertor leg remains excitation-dominated, whereas the simulation shows recombinative contributions increasing with plasma density (not shown). This observation is consistent with the colder/denser target conditions in simulations w.r.t Langmuir probe measurements, section III B, as volumetric recombination is only expected to become important at low temperature and features a strong density dependence.

DSS Stark density measurements are unavailable as line broadening during these discharges falls below the detectable level, providing further evidence that high densities, as seen in the simulation (up to  $n_e' = 8.4 \cdot 10^{19} \text{ m}^{-3}$ ), are not attained in the considered discharges #67162 and #67256.

## 2. Carbon lines

The predominant volumetric heat sinks in our simulations are impurity radiation and electron-neutral interaction (including  $D^0$  ionisation and dissociation of  $D_2$ ). Here we attempt to examine the carbon content by comparing the intensities of the CII 426.8 nm line emitted by  $C^+$ -ions in the divertor, Figure 15, as the often employed CIII-line at 465.0 nm is not monitored for these discharges. The simulated carbon emis-

sion along the divertor leg exceeds the measurement by factor  $\sim 2$ , which is qualitatively consistent with the bolometer results, section III D. This is another indication of an overestimated divertor carbon content within the simulation and/or divertor conditions more favorable to carbon radiation as discussed above. However, the notion of an overestimated divertor carbon content contradicts the upstream CXRS measurements where lower carbon levels are found in the simulation, cf. section III D.

The simulations show the CII emission front retracting towards the X-point with increasing plasma density, as the corresponding energy level occupation by electron excitation is strongly suppressed below a certain local electron temperature  $T_e$ . Experimentally, detachment of the CII emission from the target is not observed, whereas its peak intensity profile flattens, indicating some cooling at the strike point.

The SOLPS-ITER simulations can be used to generate a relation between carbon front location of CII and CIII, employing the 90% quantile front criterion as described in<sup>5</sup>, to the  $T_e$ -front position, Figure 16. The simulation relates the CIII 465.0 nm-front position to a local  $T_e$  in the range of 7 – 10 eV and the CII 426.8 nm-front in the range 2 – 5 eV. For  $\langle n_e \rangle_l = 9.5 \cdot 10^{19} \text{ m}^{-3}$ , Figure 15, the simulated CII-front corresponds to a temperature  $\sim 3$  eV, whereas the measured CII-signal remains attached to the target indicating a higher  $T_e$ . The DSS measurements, thus, qualitatively support the Langmuir probe observations. MANTIS measurements show that the CIII-front detaches from the outer target during the density ramp (not shown), providing an upper bound for  $T_e'$  of

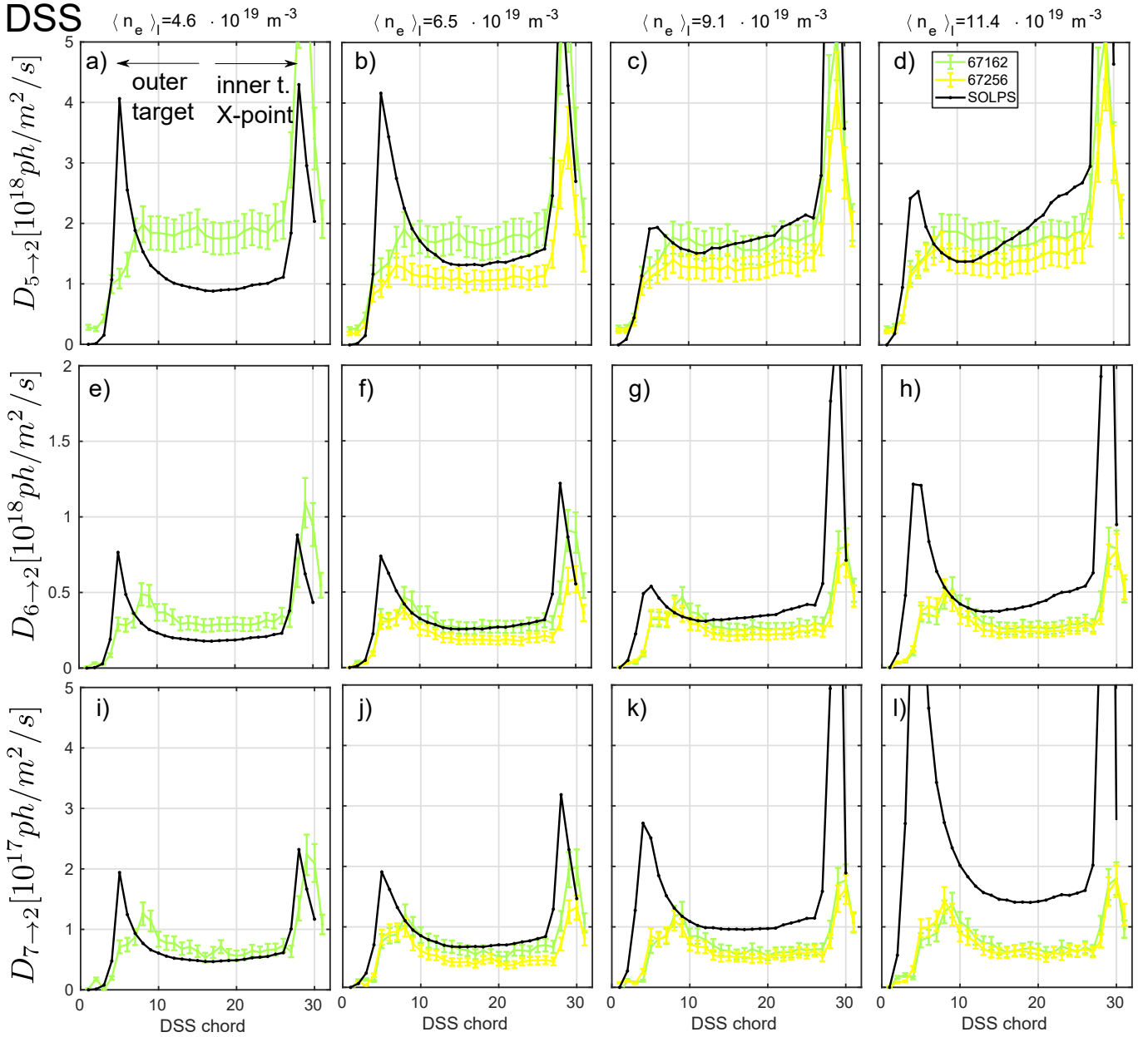


FIG. 14. Balmer line comparison between DSS and synthetic diagnostic, chords are numbered starting from the lowest DSS chord corresponding to the location close to the outer target and ascending towards the X-point/inner target

10 eV (see Figure 16) which is compatible with the bulk of the LP measurements, cf. Figure 10 h.

#### F. Simultaneous $n_e, T_e$ -comparison in four poloidally separated regions

The density ramp experiments discussed above indicate that the simulations underestimate  $T_e'$  and overestimate  $n_e'$  when compared with Langmuir probe measurements. Langmuir probes are, however, prone to misinterpretation in low  $T_e$  condition, where the electrons in the high energy tail of their distribution function contribute over-proportionally to the I-

V characteristics leading to an overestimation of  $T_e$ , cf.<sup>18</sup> and references therein. To check the Langmuir probe estimates, and further assess cross-field transport in the divertor leg, simultaneous measurements of  $n_e$  and  $T_e$  profiles along the divertor leg are performed at four poloidally separated locations employing Thomson scattering (TS), the reciprocating probe (RCP) and Langmuir probes (LP).

TS provides SOL profiles at three viewing chord intersections with the separatrix: two in the upper SOL at the upper and lower part of the main plasma and one in the divertor. The upper intersection with the separatrix is not employed here as the corresponding polychromators are not optimised for the edge plasma and obtain poor signal-to-noise ratio in the

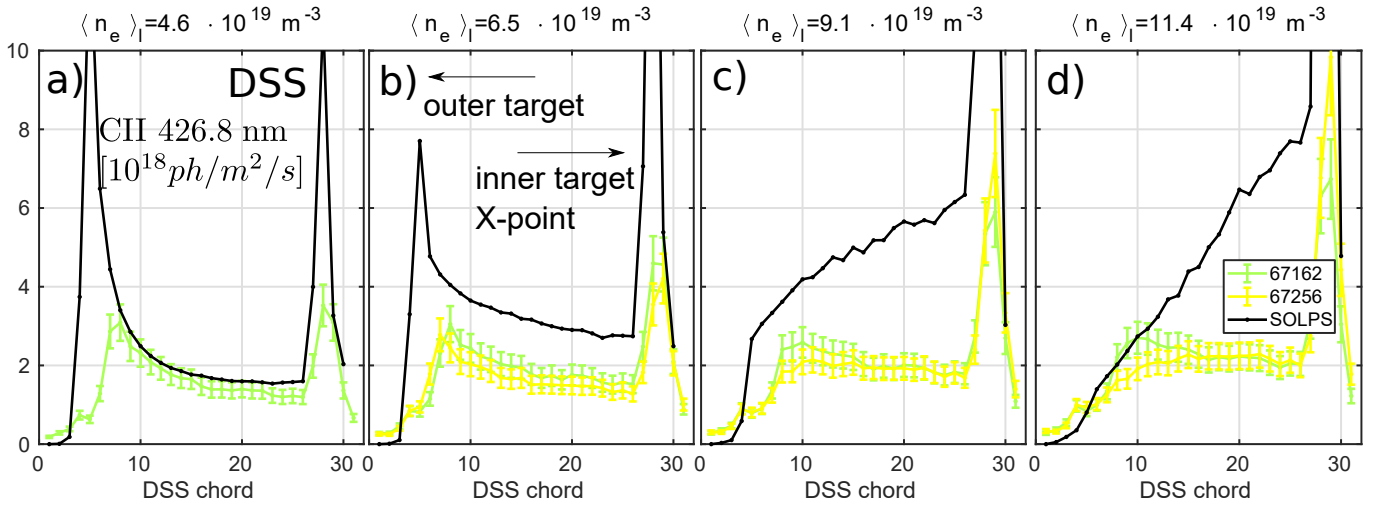
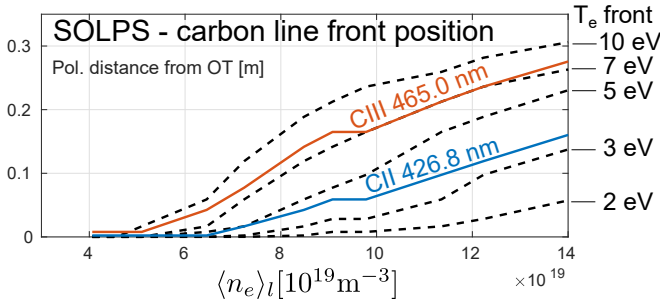


FIG. 15. CII (426.8 nm) comparison between DSS and synthetic diagnostic

FIG. 16. Evolution of carbon radiation front positions in SOLPS density scan. Front criterion: 90% quantile as done in<sup>5</sup>

edge for our discharges, whereas the TS system at the lower separatrix intersection, marked as ① in Figure 17a, features high spatial resolution in the edge. The reciprocating probe was mounted on the lower lateral port providing measurements below the X-point ②. RCP measurements are binned in 40 bins of width  $\sim 1.1$  mm for better contrast. The lowest TS measurement volume,  $\sim 6$  cm above the vessel floor, provides a third poloidal measurement location ③. The TS lasers are operated in simultaneous triggering mode to ensure sufficient collected light limiting the pulse rate to 20 Hz. A slow strike point sweep with low amplitude is used to generate a radial divertor TS profile. These discharges were taken at fixed line-averaged density in the range  $\langle n_e \rangle_l = 4 \cdot 10^{19} \text{ m}^{-3}$  to  $9 \cdot 10^{19} \text{ m}^{-3}$  to obtain many sample points at a given density. Voltage-swept LPs provide the fourth poloidal measurement location ④.

This is the first time the upgraded TCV divertor TS spectrometers<sup>22</sup> are used in a quantitative comparison with simulations and other diagnostics. TS measurements are averages over volumes defined by the width of the laser beam and the imperfect superposition of the three laser beams in the divertor, of an estimated radial width of  $\Delta R \approx 18.3$  mm and a vertical height of  $\Delta Z = 12$  mm. The resulting radial displacement, i.e. perpendicular to magnetic flux surfaces is obtained

geometrically,

$$dr = \sqrt{\Delta R^2 \cos^2 \beta_\theta + \Delta Z^2 \sin^2 \beta_\theta} \quad (5)$$

with poloidal leg tilt-angle  $\beta_\theta$ , here  $\beta_\theta \approx 18^\circ$ . Upstream mapping results in a radial measurement volume extent  $dr^u = dr/f_{exp}$  reduced by the poloidal flux expansion  $f_{exp}$ , here  $f_{exp}^{ot} \approx 3$ . For our discharges,  $dr^u \approx 5.9$  mm. Possible uncertainties in the separatrix position are neglected as these are likely smaller as the profiles in the various poloidal positions align well with each other.

First, the measurements of electron temperature  $T_e$  are considered, Figure 17b-e. At the upstream location ①, Figure 17b, the SOLPS simulations agree with the measurements to within the experimental scatter, but notably lie at the higher end of that scatter. Also here, the previously seen trend of lower  $T_e$  with higher  $n_e$  is clear, cf. Figure 4. At the RCP plunge below the X-point ②, Figure 17c, the simulation profiles also agree well with measurement with both the peak values and radial falloff lengths in both radial directions matched. At the divertor TS location above the target ③, Figure 17d, the profiles are still reasonably matched in absolute value and radial width. However, at the outer target ④, Figure 17e, the simulations yield a  $T_e^t$  systematically lower than measured by LPs, whereas LPs yield temperatures that are comparable to divertor TS results,  $T_e^{t,max} \approx 18$  eV (low density) and  $T_e^{t,max} \approx 10$  eV (high density). The profile shape is, however, still reproduced at low density.

Next, the measurements of electron density  $n_e$  are considered, Figure 17f-i. At the upstream location ①, Figure 17f, the SOLPS simulations agree with the measurements in the SOL to within the experimental scatter. At the RCP plunge below the X-point ②, Figure 17g, deviations between simulations and the measurement are evident. The peak value is underestimated and the decay lengths towards CFR and PFR overestimated. The high density case also features a narrow peak, that is attributed to drifts, as it is absent in simulations

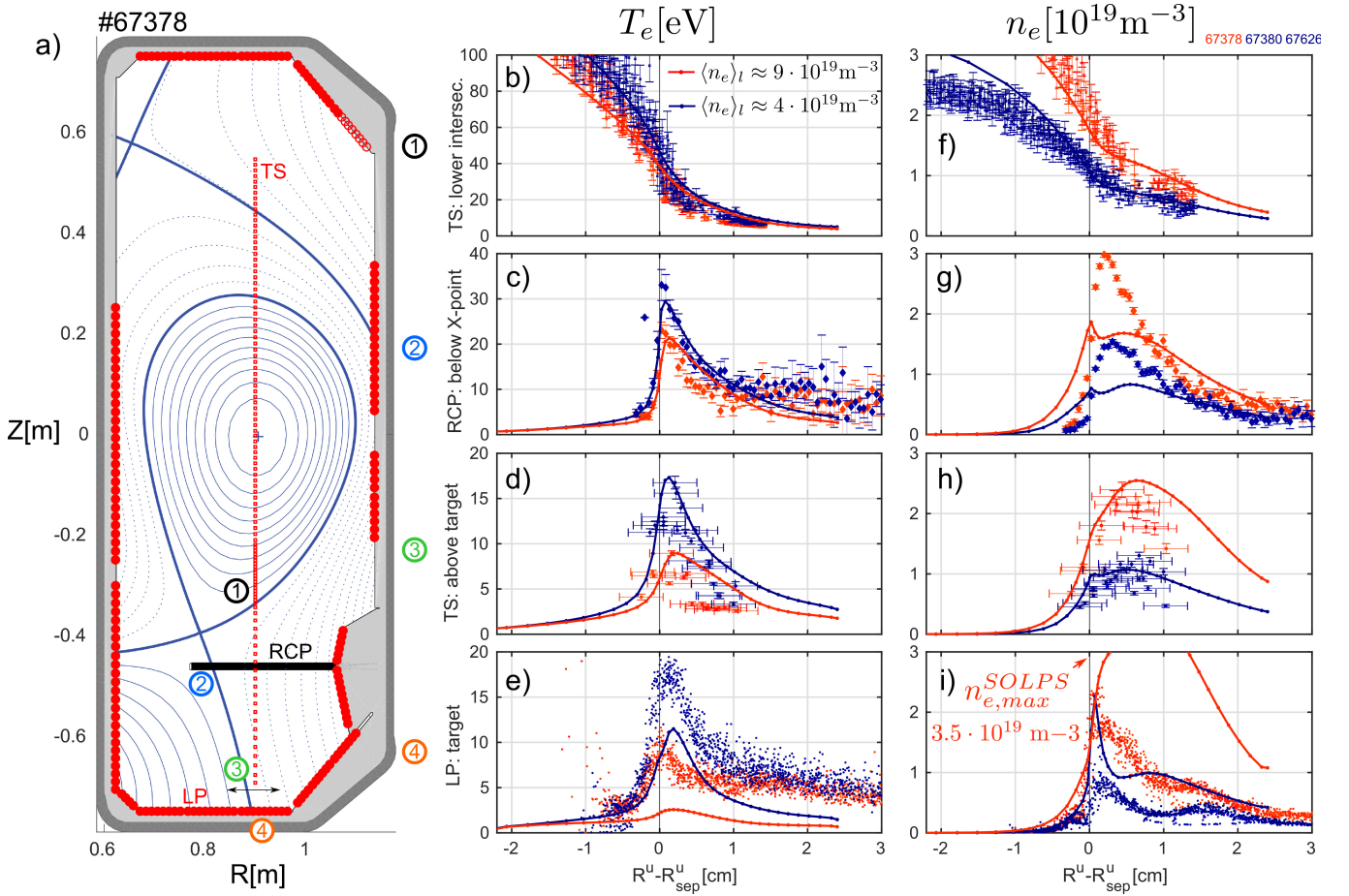


FIG. 17. Comparison of electron density  $n_e$  and temperature  $T_e$  profiles in several poloidal positions: a) plasma geometry with upstream TS intersection ①, RCP plunge ②, divertor TS ③ and wall-mounted LPs ④, b-e) corresponding  $T_e$  profiles and f-i)  $n_e$  profiles. MDS numbers SOLPS: 179196, 176913

without drifts but is, however, absent in experimental profiles. At the divertor TS location above the target ③, Figure 17h, the peak value is again consistent with the measurement, whereas the simulated profile is broader than experimentally observed. At the outer target ④, Figure 17i, the density is overestimated w.r.t. wall-mounted LPs and here the profile width is overestimated for the high density case.

The measurements indicate that the poloidal density and temperature gradients are weak between positions ③ and ④. Spectroscopic measurements employing MANTIS indicate that, in both discharges, the CHII-front does not strongly detach from the target (not shown) confirming that the experimental target temperature  $T_e^{t,max} > 7$  eV, cf. Figure 16, is indeed underestimated by the simulation ( $T_e^{t,max} = 2.6$  eV). The strong poloidal  $T_e$  and  $n_e$  gradients close to the target in the simulation may possibly explain the stronger outer target Balmer line emission near the target w.r.t the DSS measurements, Figure 14. Upon searching for reactions in the simulations in the considered volume close to the target that provide significant contribution to the balance equations, we find significant momentum losses from atomic charge-exchange and power losses from electron-molecule reactions (not shown).

This suggests a link to the overestimated divertor neutral pressure, section III C, as the strength of these reactions is proportional to the divertor neutral density. Attempts to reconcile the simulated and measured divertor neutral pressure are discussed in section IV D.

RCP, divertor TS and LPs consistently indicate that the density profile width is overestimated by the simulation. In simulations without drifts this can be easily adjusted by locally reducing anomalous transport coefficients. However, improvement of the match to the experimental profile was not achieved in these drift simulations upon reduction of  $D_{\perp}^{AN}$  and  $\chi_{\perp}^{AN}$  by up to factor 4 (not shown), consistent with the finding that the radial particle transport in the simulation is  $E \times B$ -dominated, as discussed in<sup>23</sup>. Simulations without drifts do not feature the density peak near the separatrix seen in Figure 17 g,i, that becomes more pronounced in those simulations where anomalous transport is reduced further. The underlying reason for the overestimated density profile width remains elusive. Possible candidates are a) an overestimation of the  $E_{\theta} \times B_{\phi}$ -transport, b) an underestimation of the parallel flow or c) an overestimation of the width of the particle source  $S_{part}$ . Option c) may be discarded as recent measure-

ment of the volumetric ionisation source with the MANTIS diagnostic<sup>10</sup> show reasonable agreement to the simulated ionisation profiles. Option b) may be discarded as the integrated target particle flux is reasonably well captured by the simulations, Figure 5. Presently, option a) seems most likely and is supported by the observation that  $T_e^t$  is lower in the simulations w.r.t to the measurements, thus leading to larger  $E_\theta$  in the simulations. We remark that the electrostatic potential in these simulations and the experiments remains positive (confirmed by the RCP plunge), contrary to the baffled discharges at higher  $I_p$  and  $\langle n_e \rangle_l$  where lower  $T_e^t$  was obtained and a potential well structure was measured<sup>14</sup>.

Presently, it is thought that the discrepancies regarding overestimated target density  $n_e^t$ , radial  $E_\theta \times B_\phi$ -transport, divertor neutral pressure and the underestimated target temperature  $T_e^t$  are linked to each other, e.g. a lower divertor neutral content would imply lower  $n_e^t$ , higher  $T_e^t$  and thus smaller  $E_\theta$ . At this stage the underlying reason(s) for the discrepancies remain elusive and it cannot be concluded whether the quantitative disagreement is caused by poor simulations settings or missing or inaccurately treated mechanisms in the SOLPS-ITER model itself.

#### IV. COMPARISON - BAFFLED TCV

We apply the same analysis to nominally identical TCV discharges with installed divertor baffles. The first baffled TCV campaign immediately demonstrated higher divertor neutral pressure facilitating access to detachment<sup>7,8</sup>. Generally, the comparison between simulations and experiments with installed baffles yields the same conclusions: the simulated divertor neutral pressure is higher, and the outer divertor is colder and denser than experimentally observed for matched upstream conditions. Here, we focus on a few selected aspects: the evolution of upstream parameters, section IV A, the target particle flux roll-over, section IV B, spectroscopic measurements, section IV C, and the divertor neutral pressure in section IV D. The considered discharges and simulations are summarised in Table II a.

A phenomenon, that is only observed in baffled discharges, is an abrupt increase in  $\langle n_e \rangle_l$  during the density ramp, with a simultaneous stagnation in divertor neutral pressure, indicating a loss of plasma plugging, after which  $p_n^{div}$  is comparable to unbaffled discharges. The phenomenon was named BURP (*aBrupt Unexpected Reduction of Plasma plugging*)<sup>8</sup>. The BURP does, however, not occur for all baffled discharges and appears to be a dynamic process. Discharges with BURPs are therefore excluded from the analysis as only the stationary plasma solutions are modelled herein.

##### A. Upstream plasma parameters

In unbaffled discharges, where high divertor neutral pressures are attained  $p_n^{div}$  (#65903 and #66092) a drop of upstream density, temperature and pressure is observed towards the end of the density ramp, Figure 2, 4. This is also seen in

the high pressure baffled discharges considered here (#63546, #64623 and #64626), when  $p_n^{div} \approx 50$  mPa is exceeded, but considerably more pronounced w.r.t. the unbaffled case, Figure 18. These discharges feature a strong reduction in upstream temperature and pressure and are accompanied by a cold/dense radiating region on the HFS observed by the MANTIS system<sup>10,24</sup>. These features are not observed in discharges with lower  $p_n^{div} < 50$  mPa. For similar  $\langle n_e \rangle_l$  evolution we find at least two plasma class states: those with and without collapsed upstream profiles. Below we show that the upstream profile collapse in the present discharges is correlated with the target particle flux roll-over.

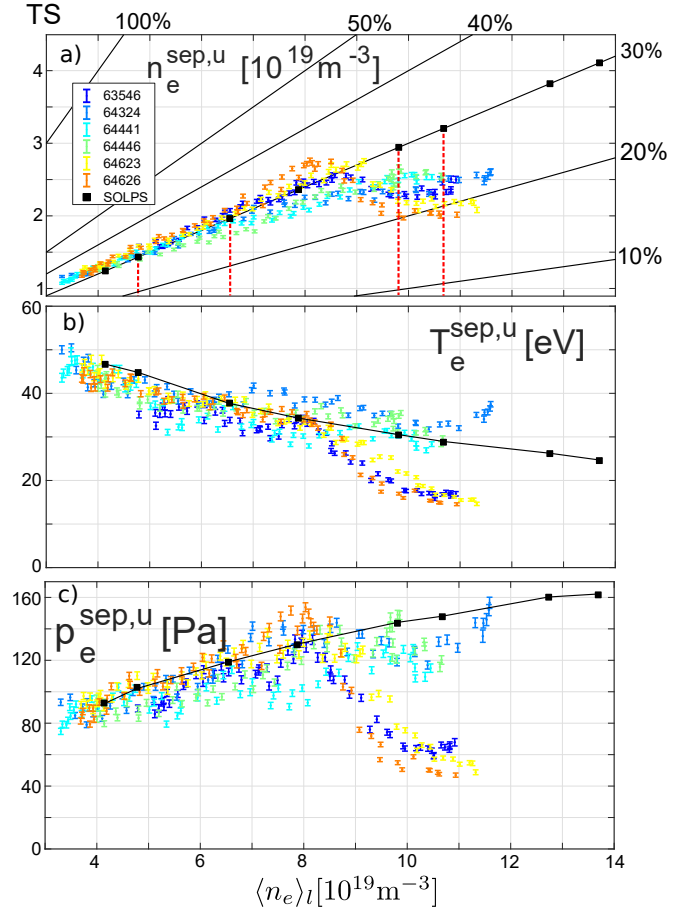


FIG. 18. Comparison of upstream separatrix  $n_e, T_e, p_e$  in baffled PEX discharges as inferred by Thomson scattering at the lower intersection with the separatrix. Red dashed lines mark the positions where profiles are compared in the following.

We find that the separatrix density stagnates at  $n_e^{sep,u} \approx 2.8 \cdot 10^{19} \text{ m}^{-3}$  in these baffled discharges, Figure 18a. Further gas fuelling only increases  $\langle n_e \rangle_l$  but not  $n_e^{sep,u}$ . This  $n_e^{sep,u}$  saturation does, however, not appear in SOLPS simulations. Although fuelling rates in baffled and unbaffled discharges are comparable (not shown), baffled simulations require up to factor 3 higher fuelling to obtain this  $n_e^{sep,u}$  to compensate for an increased divertor neutral pumping. The saturation of  $n_e^{sep,u}$  in the baffled experiment above  $\langle n_e \rangle_l > 8 \cdot 10^{19} \text{ m}^{-3}$  is presently not understood.

## a) PEX experiments - with baffles

#shot	BAR	BOLO	TS	CXRS	VIR	HIR	LP	RCP	RDPA	DSS	MANTIS
63546	█	█	█	█	█	█	█	█	█	█	█
64324	█	█	█	█	█	█	█	█	█	█	█
64441	█	█	█	█	█	█	█	█	█	█	█
64446	█	█	█	█	█	█	█	█	█	█	█
64623	█	█	█	█	█	█	█	█	█	█	█
64626	█	█	█	█	█	█	█	█	█	█	█

## b) SOLPS simulations - with baffle

gas puff $\Gamma_{D_2}$ [ $10^{20}$ D <sub>0</sub> /s]	7	10	15	20	25	30	35	40
$n_e^{sep,omp}$ [ $10^{19}$ m <sup>-3</sup> ]	1.24	1.43	1.96	2.36	2.94	3.20	3.80	4.11
MDS number	169206	175209	150140	150141	151651	150142	181756	150143

TABLE II. TCV discharges without baffles and diagnostic availability (red=no data available, green=data acquired), b) SOLPS-ITER density scan with separatrix density at the outer midplane  $n_e^{sep,omp}$  and MDS number.

## B. Target particle flux roll-over

The measured target particle flux shows a clear roll-over, only in those discharges where the upstream pressure drops and a divertor pressure of 50 mPa is exceeded, Figure 19. In contrast to discharges without baffles, the inner target also shows a roll-over. Spectroscopic measurements with DSS indicate that atomic recombination contributions in the divertor particle balance remain small. The target particle flux roll-over in these TCV discharges is therefore attributed to a collapse in the upstream profiles rather than volumetric divertor particle sinks. The simulation supports this notion, as recombination rates remain negligible for the particle balance in the divertor, despite the likely underestimated target temperatures that drop below  $T_e^t < 1$  eV, saturating the ionisation source that leads to a stagnating target particle flux at high plasma density. Even when the modelled density is increased beyond the experimentally accessible values (20% higher) the simulation does not see any roll-over.

Previous simulation work by Wischmeier<sup>25</sup> on TCV suggested a link between the target particle flux roll-over and increased impurity sputtering from the main chamber. This was thought to result from a broadening of the density profile in the far-SOL with increasing plasma density. Such a main chamber source could then contribute to the collapse of the upstream profiles at high density and reconcile the carbon densities in the core-edge region with CXRS measurements. Such a main chamber release would, however, also alter the radiation profile in the edge, that does agree well with our simulations with the carbon source in the divertor, cf. Figure 13.

Recent spectroscopic investigations by Verhaegh<sup>26</sup> propose molecular-activated recombination (MAR) as an additional volumetric particle sink comparable to the reduction in target particle flux for TCV's density ramps. MAR describes the recombination of electrons with  $D_2^+$  ions that are created, either by molecular ionisation, or molecular charge-exchange. While these reactions are principally included in our simulations, it is argued that the production of  $D_2^+$  may be strongly

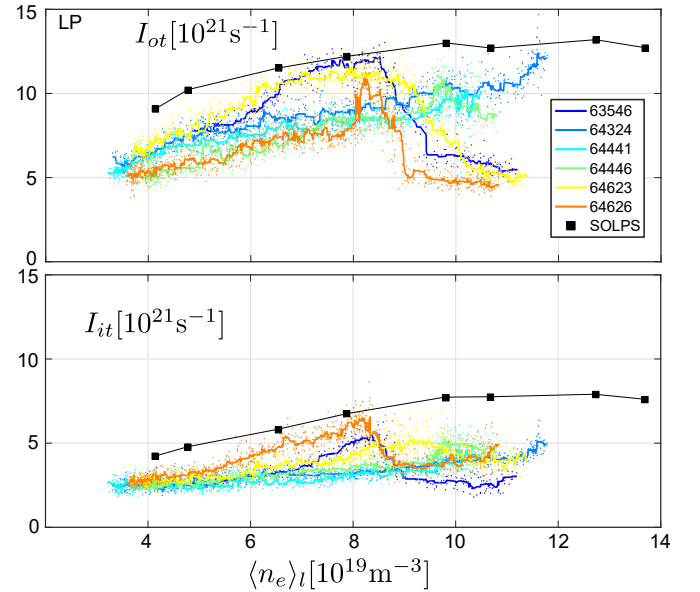


FIG. 19. Comparison of ion target current in the baffled TCV divertor

underestimated.

## C. Spectroscopic comparison

In the following, spectroscopic evidence will be presented that supports a colder/denser divertor w.r.t. the unbaffled TCV divertor, discussed in section III E. DSS measurements in the baffled divertor are compared for the  $D_{5 \rightarrow 2}$  line, Figure 20 a-d,  $D_{6 \rightarrow 2}$ , Figure 20 e-h,  $D_{7 \rightarrow 2}$ , Figure 20 i-l, CII (426.8 nm), Figure 20 m-p and CIII (465.0 nm), Figure 20 q-t. This measurement employed the 2019 DSS field of view that excluded the inner strike point. Four DSS chords were also blocked by the port structure, indicated by a gray shaded region in Figure 20.

While the  $D_{6 \rightarrow 2}$  and  $D_{7 \rightarrow 2}$  intensities match reasonably

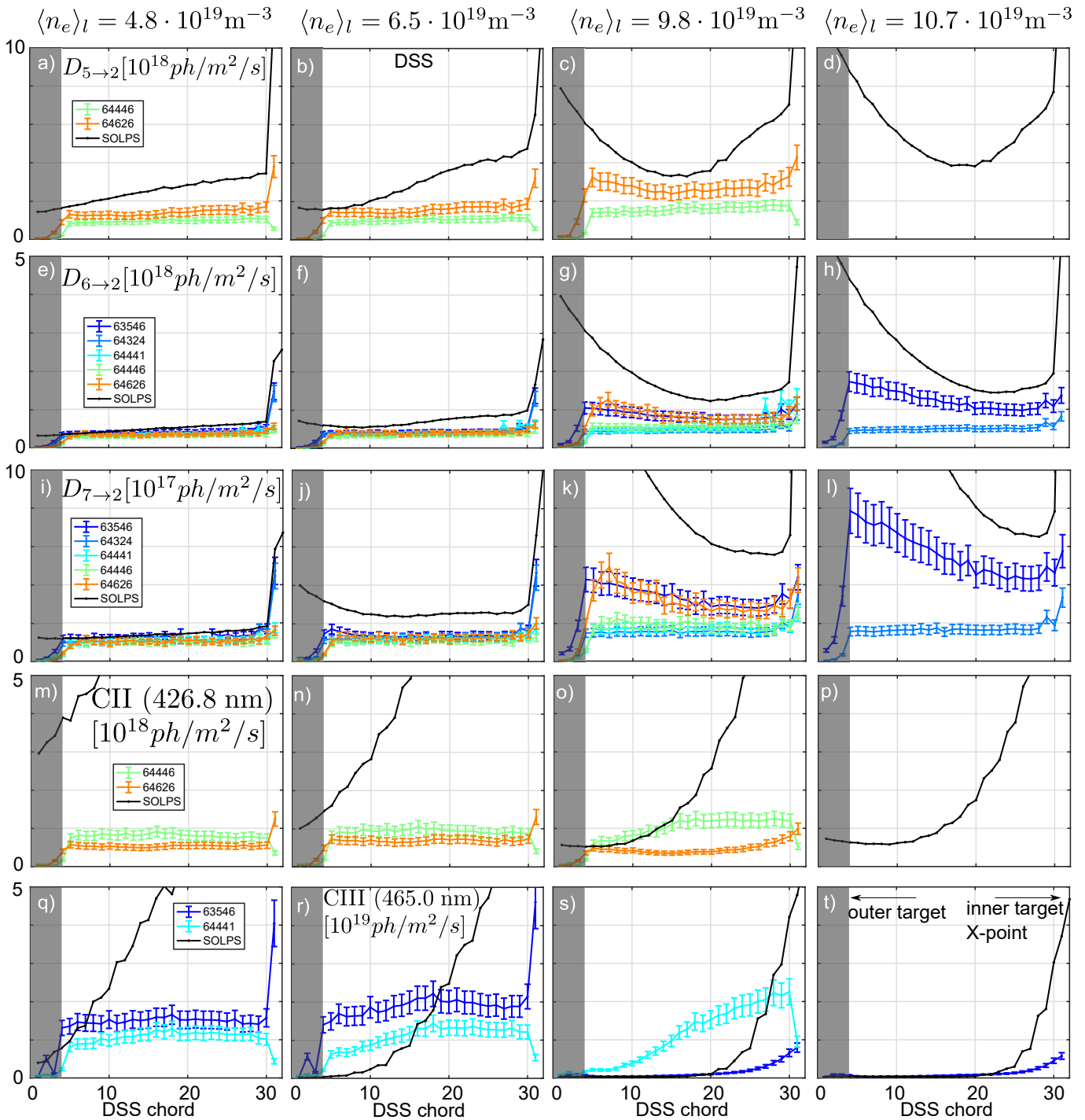


FIG. 20. Spectroscopic comparison of Balmer and Carbon lines in baffled TCV discharges between DSS measurements and corresponding SOLPS-ITER simulations. The gray-shaded DSS chords are shadowed by the diagnostic port and do not see the plasma.

well at low density the  $D_{5 \rightarrow 2}$  intensity exceeds the simulation values, 20 a,e,i, that may be attributed to radiative contributions from molecular processes or uncertainties in the calibration on the DSS as the simulated emission at  $\langle n_e \rangle_l = 4.8 \cdot 10^{19} \text{ m}^{-3}$  is excitation-dominated. With increasing density, the recombinative contribution to Balmer line emission increases in cold regions leading to enhanced Balmer radi-

ation near the outer target. In the simulations, this occurs at lower  $\langle n_e \rangle_l$  and is more pronounced than in the experiment again indicating colder/denser target conditions in the simulation, Figure 20g,k, that is consistent with the conclusions above in the absence of divertor baffles. Notably, experiments show a large variation at the higher densities indicating that the line-averaged density  $\langle n_e \rangle_l$  and the upstream den-

ity  $n_e^{sep,omp}$  are both becoming a poorer ordering parameter to characterize the divertor state.

The carbon line intensities and corresponding front movements during the density ramps are now addressed. Measurements of the CII (426.8 nm) and the CIII (465.0 nm) lines are available for a subset of baffled discharges. As for the unbaffled cases, section III E, higher simulated carbon emission in the divertor is modelled than experimentally measured by the DSS. However, from bolometry, the experimental  $p_{rad}^{SOL}$  exceeds the simulation by up to 30% (not shown) and now shows reasonable agreement with the divertor channels.

The retraction of the simulated carbon fronts from the target sets in at lower density than experimentally observed, again indicating an underestimated simulated divertor temperature. The measured CII-emission does not detach from the target with increasing density, although there was some profile deformation observed with increasing plasma density, Figure 20o. This suggests that the experimental target temperature  $T_e^t$  does not fall below 2 eV in the discharges. The CIII-front shows clear retraction towards the X-point in the experiments for the cases at high density, again with large differences between discharges that reach different  $p_n^{div}$ , Figure 20s.

#### D. Divertor neutral pressure

The predicted increase of divertor neutral pressure with baffles<sup>5</sup> is qualitatively confirmed by TCV measurements, Figure 21. However, simulations yield systematically higher  $p_n^{div}$  by factor  $\sim 4$ , as discussed for the unbaffled cases, section III C.

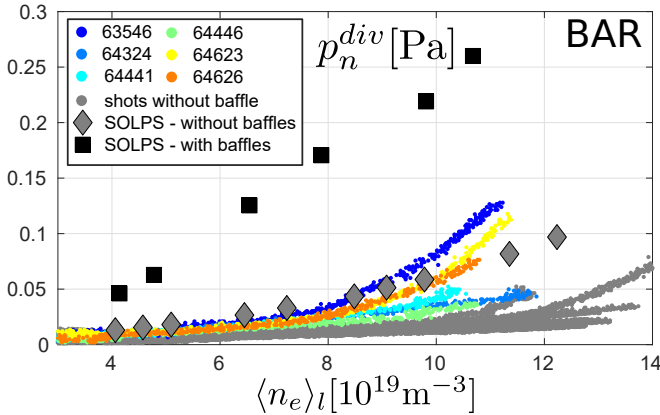


FIG. 21. Divertor neutral pressure  $p_n^{div}$  as measured by the divertor baratron gauge for the baffled and unbaffled TCV divertor.

Attempts to reconcile experimental and simulated divertor pressure by varying the recycling coefficients  $R = 1 - p_p$  for various species proved unsuccessful. Wall pumping in our simulations with species-independent recycling coefficient  $R = 0.99$  (chosen constant for all PFCs) is predominantly determined by the pumping of molecules on the walls of the divertor chamber. Modification of the recycling coefficient alone is insufficient to reduce  $p_n^{div}$  as  $R$  also affects the upstream density for a given gas puff. Further adjusting the gas

puff to attain similar upstream profiles then yields nearly identical target conditions and  $p_n^{div}$  for different sets of recycling coefficients (not shown). The effect on the simulated  $p_n^{div}$  for a range of recycling coefficients for the particle species is now discussed. Simulations with disabled molecular pumping  $R_{mol} = 1$  or strongly increased neutral pumping  $R_{neutral} = 0.95$  reduce the neutral pressure only modestly yet still exceed the measurements by factor  $\sim 3$  for a given plasma density  $\langle n_e \rangle_l$ . The strongest decrease of  $p_n^{div}$  is achieved by reducing transport coefficients ( $D_{\perp}^{AN} = 0.2 \rightarrow 0.15$  and  $\chi_{\perp}^{AN} = 1.0 \rightarrow 0.5$ ), but still fails to reproduce the experiment, Figure 22. The baratron divertor neutral pressure is not a direct SOLPS output but requires postprocessing through the synthetic baratron model whose benchmark with Eirene results shows deviations of less than 20%, i.e. far less than that needed to explain the discrepancy, cf. Appendix in<sup>5</sup>. Accounting for the finite baratron reponse time  $\tau_{delay} \approx 60$  ms in these experiments results in a density shift of measurements  $\delta \langle n_e \rangle_l \approx 4 \cdot 10^{18} m^{-3}$ , i.e. a horizontal shift in Figures 21, 22 (not shown), again insufficient, by far, to reconcile simulation and measurement.

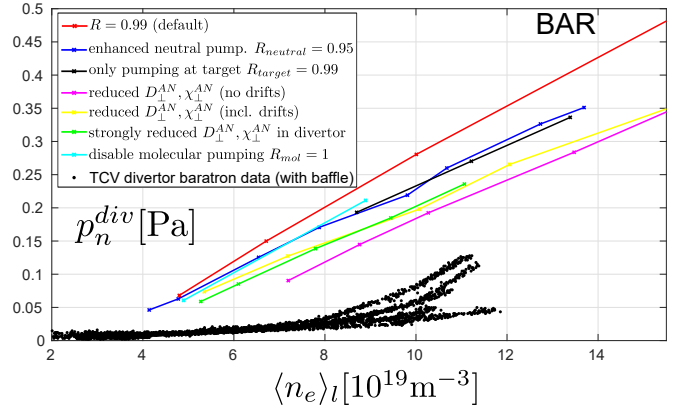


FIG. 22. Attempts to reconcile experimental and simulated divertor neutral pressure for the baffled TCV divertor.

The overestimation of  $p_n^{div}$  is likely linked to the overestimated  $n_e^t$  and underestimated  $T_e^t$  as it precludes increased plasma-neutral interaction. A link to the likely overestimated divertor carbon content is less clear, as simulations with strongly altered carbon content, change  $p_n^{div}$  little (not shown).

The reason for the mismatch in divertor neutral pressure remains elusive. The installation of additional, more sensitive, diagnostics for neutral pressure measurements (ASDEX-gauges) is underway on TCV and will help probe the discrepancy further.

#### V. CONCLUSIONS

This work summarizes a first full experimental comparison of SOLPS-ITER drift simulations for L-mode discharges in the TCV tokamak. The comparison employs the line-averaged density  $\langle n_e \rangle_l$  as ordering parameter. The only parameter varied in the simulations is the gas puff, whereas anomalous

transport coefficients, carbon chemical sputtering yield, wall recycling coefficients and heating power are fixed.

These simple assumptions yield simulations that reasonably well model the experimental  $n_e$  and  $T_e$  upstream profiles across the density scan. Despite large experimental uncertainties at the edge, CXRS measurements indicate an underestimated ion temperature  $T_i$ , suggesting simulations with modified electron/ion heat sharing on the core  $P_e^{core}/P_i^{core} < 1$  in future studies. The total target particle flux, and its in/out asymmetry, are reasonably well reproduced, whereas the outer target profile shape is not but indicates overestimated radial transport in the simulations. A clear roll-over in the target particle flux is not observed in the unbaffled scenario considered in this work nor in corresponding simulations. A comparison of target heat flux profiles showed experimental deviations between Langmuir probes and infrared cameras that could not be resolved in this work. The modelled heat flux profile shape at the target is similar to the experimental profiles, albeit with different amplitudes, and thus, unsurprisingly with a difference in the in/out power symmetry. The comparison to Langmuir probes indicates overestimated  $n_e'$  together with underestimated  $T_e'$  in the simulations, consistent with overestimated  $P_{rad}^{SOL}$  (BOLO), larger recombinative contribution to Balmer line emission at high density (DSS) and the lack of CII-front movement in the experiment (DSS).

Simultaneous measurements at four poloidally separated positions in the TCV edge, employing main SOL and divertor TS, RCP and wall-mounted Langmuir probes, allow a stringent comparison of density and temperature profiles in the SOL. This indicates a higher simulated density width in the divertor leg, starting below the X-point region and translating forward towards the outer target, whereas the temperature profile shape is accurately described at all locations but displays a lower peak temperature w.r.t. wall-mounted Langmuir probes. This indicates an overestimated radial particle transport caused by the  $E_\theta \times B_\phi$ -drift as consequence of overestimated poloidal temperature gradients from the colder/denser target. The comparison reveals overestimated poloidal gradients of  $n_e$  and  $T_e$  in the volume  $\sim 6$  cm before the outer target in the simulation w.r.t. the experiment, which are argued to be possibly related to plasma-neutral interaction by charge-exchange and electron-molecular interactions in the corresponding volume that suggest a link to the overestimated divertor neutral pressure. Overestimated target density  $n_e'$  and underestimated temperature  $T_e'$  have also been reported for previous SOLPS simulations for ASDEX-Upgrade by Chankin<sup>27</sup> and Aho-Mantila for reversed  $B_\phi$ <sup>28</sup>.

BOLO and DSS indicate overestimated divertor (carbon) radiation in the simulation, again resulting in a colder, denser divertor state. This hints either at an overestimated carbon content or more favorable conditions for radiative losses (in line with the overestimated density). Contrary to the apparently overestimated carbon content in the divertor, CXRS finds up to one order of magnitude higher carbon ( $C^{6+}$ ) densities in the core edge region. These results may possibly be reconciled by noting that  $C^{6+}$  production in the core, by ionisation beyond the computational core boundary, is neglected. Simulations with modified impurity boundary condition on

the core are suggested in future studies. A robust experimental power balance, following the recent bolometry system upgrade and ongoing work on the infrared cameras, would help further to constrain the simulated carbon content.

The mechanism leading to the observed target current roll-over on TCV remains elusive. A strong roll-over is only observed in these baffled discharges at high  $p_n^{div}$  and is accompanied by a simultaneous collapse in the upstream density, temperature and pressure profiles. However, simulations only find a stagnation of the ionisation source and, consequentially, a stagnation of the target particle flux, despite modelling target temperatures well below  $< 1$  eV. The underlying reason for the collapse of the upstream profile is likely linked to a strongly radiating region on the HFS<sup>10</sup>.

The comparison with the baffled TCV divertor qualitatively confirms the previously predicted increase in divertor neutral pressure  $p_n^{div}$  whereas the absolute value is overestimated by factor  $\sim 4$  in simulations. It was not possible to reconcile experimental and simulated  $p_n^{div}$  by simple modification of the wall recycling coefficients nor by modifying the anomalous transport. The overestimated neutral pressure thus remains an open issue. Additional pressure gauges are foreseen for TCV installation that may clarify this mismatch.

The stringent comparison to TCV diagnostics confirms a large majority of the qualitative trends seen in simulations and, thus, the validity of the main underlying physics model in the SOLPS-ITER code. It also highlights remaining discrepancies that require further attention. While the SOLPS-ITER results of these TCV discharges seem to be overly optimistic in terms of divertor cooling and detachment access, a conclusion on the consequences for next-level fusion devices cannot be drawn as the responsible mechanism(s) for these deviations remain elusive.

## DATA AVAILABILITY STATEMENT

The data that support the findings of this study are available from the corresponding author upon reasonable request.

## ACKNOWLEDGMENTS

This work was carried out within the framework of the EUROfusion Consortium and has received funding from the Euratom research and training programme 2014–2018 and 2019–2020 under Grant Agreement No. 633053. The views and opinions expressed herein do not necessarily reflect those of the European Commission. This work was supported in part by the Swiss National Science Foundation. This work was supported in part by the US Department of Energy under Award Number DE-SC0010529.

<sup>1</sup>A. Kukushkin, H. Pacher, V. Kotov, G. Pacher, and D. Reiter, “Finalizing the ITER divertor design: The key role of SOLPS modeling,” *Fusion Engineering and Design* **86**, 2865–2873 (2011).

<sup>2</sup>L. Aho-Mantila, S. Potzel, D. P. Coster, M. Wischmeier, M. Brix, R. Fischer, S. Marsen, A. Meigs, H. W. Müller, A. Scarabosio, M. F. Stamp, S. Brezinsek, and and, “Assessment of SOLPS5.0 divertor solutions with

- drifts and currents against I-mode experiments in ASDEX upgrade and JET,” *Plasma Physics and Controlled Fusion* **59**, 035003 (2017).
- <sup>3</sup>H. Reimerdes, S. Alberti, P. Blanchard, P. Bruzzone, R. Chavan, S. Coda, B. Duval, A. Fasoli, B. Labit, B. Lipschultz, T. Lunt, Y. Martin, J.-M. Moret, U. Sheikh, B. Sudki, D. Testa, C. Theiler, M. Toussaint, D. Uglietti, N. Vianello, and M. Wischmeier, “TCV divertor upgrade for alternative magnetic configurations,” *Nuclear Materials and Energy* **12**, 1106–1111 (2017).
  - <sup>4</sup>A. Fasoli, H. Reimerdes, S. Alberti, M. Baquero-Ruiz, B. Duval, E. Havlikova, A. Karpushov, J.-M. Moret, M. Toussaint, H. Elaian, M. Silva, C. Theiler, and D. V. and, “TCV heating and divertor upgrades,” *Nuclear Fusion* **60**, 016019 (2019).
  - <sup>5</sup>M. Wensing, B. Duval, O. Février, A. Fil, D. Galassi, E. Havlickova, A. Perek, H. Reimerdes, C. Theiler, K. Verhaegh, and M. Wischmeier, “SOLPS-ITER simulations of the TCV divertor upgrade,” *Plasma Physics and Controlled Fusion* **61** (2019), 10.1088/1361-6587/ab2b1f.
  - <sup>6</sup>D. Galassi, H. Reimerdes, C. Theiler, M. Wensing, H. Bufferand, G. Ciraolo, P. Innocente, Y. Marandet, P. Tamain, the EUROfusion MST1 Team, and the TCV Team, “Numerical investigation of optimal divertor gas baffle closure on TCV,” *Plasma Physics and Controlled Fusion* **62**, 115009 (2020).
  - <sup>7</sup>H. Reimerdes, B. Duval, H. Elaian, A. Fasoli, O. Février, C. Theiler, F. Bagnato, M. Baquero-Ruiz, P. Blanchard, D. Brida, C. Colandrea, H. D. Oliveira, D. Galassi, S. Gorno, S. Henderson, M. Komm, B. Linehan, L. Martinelli, R. Maurizio, J.-M. Moret, A. Perek, H. Raj, U. Sheikh, D. Testa, M. Toussaint, C. Tsui, M. Wensing, the TCV team, and the EUROfusion MST1 team, “Initial TCV operation with a baffled divertor,” *Nuclear Fusion* **61**, 024002 (2021).
  - <sup>8</sup>O. Février, H. Reimerdes, C. Theiler, D. Brida, C. Colandrea, H. D. Oliveira, B. Duval, D. Galassi, S. Gorno, S. Henderson, M. Komm, B. Labit, B. Linehan, L. Martinelli, A. Perek, H. Raj, U. Sheikh, C. Tsui, and M. Wensing, “Divertor closure effects on the TCV boundary plasma,” *Nuclear Materials and Energy* **27**, 100977 (2021).
  - <sup>9</sup>K. Verhaegh, “Spectroscopic investigations of detachment on tcv: Investigating the role of atomic physics on the ion current roll-over and the dynamics of detachment in tcv,” (2018), PhD thesis.
  - <sup>10</sup>A. Perek, M. Wensing, K. Verhaegh, B. Linehan, H. Reimerdes, C. Bowman, M. van Berkel, I. Classen, B. Duval, O. Février, J. Koenders, T. Ravensbergen, C. Theiler, and M. de Baar, “A spectroscopic comparison of the cross-field particle transport in detached conditions between the tcv tokamak and solps-iter,” (2021), in preparation.
  - <sup>11</sup>X. Bonnin, W. Dekeyser, R. Pitts, D. Coster, S. Voskoboynikov, and S. Wiesen, “Presentation of the new SOLPS-ITER code package for tokamak plasma edge modelling,” *Plasma and Fusion Research* **11**, 1403102–1403102 (2016).
  - <sup>12</sup>S. Wiesen, D. Reiter, V. Kotov, M. Baelmans, W. Dekeyser, A. Kukushkin, S. Lisgo, R. Pitts, V. Rozhansky, G. Saibene, I. Veselova, and S. Voskoboynikov, “The new SOLPS-ITER code package,” *Journal of Nuclear Materials* **463**, 480–484 (2015).
  - <sup>13</sup>M. Wensing, “Drift-related transport and plasma-neutral interaction in the TCV divertor,” (2021), PhD thesis.
  - <sup>14</sup>M. Wensing, H. de Oliveira, J. Loizu, C. Colandrea, O. Février, S. Gorno, H. Reimerdes, C. Theiler, A. Smolders, B. Duval, C. Tsui, M. Wischmeier, D. Brida, S. Henderson, and M. Komm, “Experimental verification of X-point potential well formation in unfavorable magnetic field direction,” *Nuclear Materials and Energy* , 100839 (2020).
  - <sup>15</sup>J. Bohdansky, J. Roth, and H. L. Bay, “An analytical formula and important parameters for low-energy ion sputtering,” *Journal of Applied Physics* **51**, 2861 (1980).
  - <sup>16</sup>P. Stangeby, *The Plasma Boundary of Magnetic Fusion Devices* - (Taylor & Francis, Justus-Liebig-Universität Gießen, 2000).
  - <sup>17</sup>N. Christen, C. Theiler, T. Roglien, M. Rensink, H. Reimerdes, R. Maurizio, and B. Labit, “Exploring drift effects in TCV single-null plasmas with the UEDGE code,” *Plasma Physics and Controlled Fusion* **59**, 105004 (2017).
  - <sup>18</sup>O. Février, C. Theiler, H. De Oliveira, B. Labit, N. Fedorczak, and A. Bailod, “Analysis of wall-embedded langmuir probe signals in different conditions on the tokamak à configuration variable,” *Review of Scientific Instruments* **89**, 053502 (2018), <https://doi.org/10.1063/1.5022459>.
  - <sup>19</sup>C. Marini, “Poloidal cx visible light plasma rotation diagnostics in tcv,” (2017), PhD thesis.
  - <sup>20</sup>OPEN-ADAS, “Open—Atomic Data Analysis Structure,” <https://open.adas.ac.uk/> (1995), accessed 2020-10-28.
  - <sup>21</sup>K. Verhaegh, B. Lipschultz, B. Duval, O. Février, A. Fil, C. Theiler, M. Wensing, C. Bowman, D. Gahle, J. Harrison, B. Labit, C. Marini, R. Maurizio, H. de Oliveira, H. Reimerdes, U. Sheikh, C. Tsui, N. Vianello, W. Vijvers, and and, “An improved understanding of the roles of atomic processes and power balance in divertor target ion current loss during detachment,” *Nuclear Fusion* **59**, 126038 (2019).
  - <sup>22</sup>P. Blanchard, Y. Andrebe, H. Arnichand, R. Agnello, S. Antonioni, S. Couturier, J. Decker, T. D. K. D`Exaerde, B. Duval, I. Furno, P.-F. Isoz, P. Lavanchy, X. Llobet, B. Marlétaz, and J. Masur, “Thomson scattering measurements in the divertor region of the TCV tokamak plasmas,” *Journal of Instrumentation* **14**, C10038–C10038 (2019).
  - <sup>23</sup>M. Wensing, J. Loizu, H. Reimerdes, B. Duval, M. Wischmeier, and the TCV team, “X-point potential well formation in diverted tokamaks with unfavorable magnetic field direction,” *Nuclear Fusion* **60**, 054005 (2020).
  - <sup>24</sup>A. Perek, B. Linehan, M. Wensing, K. Verhaegh, I. Classen, B. Duval, O. Février, H. Reimerdes, C. Theiler, T. Wijkamp, and M. de Baar, “Measurement of the 2d emission profiles of hydrogen and impurity ions in the TCV divertor,” *Nuclear Materials and Energy* **26**, 100858 (2021).
  - <sup>25</sup>M. Wischmeier, “Simulating divertor detachment in the TCV and JET tokamaks,” (2005), PhD thesis.
  - <sup>26</sup>K. Verhaegh, B. Lipschultz, J. Harrison, B. Duval, C. Bowman, A. Fil, D. S. Gahle, D. Moulton, O. Myatra, A. Perek, C. Theiler, and M. Wensing, “A study of the influence of plasma–molecule interactions on particle balance during detachment,” *Nuclear Materials and Energy* **26**, 100922 (2021).
  - <sup>27</sup>A. Chankin, D. Coster, N. Asakura, G. Corrigan, S. Erents, W. Fundamenski, H. Müller, R. Pitts, P. Stangeby, and M. Wischmeier, “A possible role of radial electric field in driving parallel ion flow in scrape-off layer of divertor tokamaks,” *Nuclear Fusion* **47**, 762–772 (2007).
  - <sup>28</sup>L. Aho-Mantila, M. Wischmeier, H. Müller, S. Potzel, D. Coster, X. Bonnin, and G. C. and, “Outer divertor of ASDEX upgrade in low-density I-mode discharges in forward and reversed magnetic field: I. comparison between measured plasma conditions and SOLPS5.0 code calculations,” *Nuclear Fusion* **52**, 103006 (2012).